Reflectance Measurements of Two Thin Film Materials in the UV

by

Benjamin D. Smith

A senior thesis submitted to the faculty of

Brigham Young University

in partial fulfillment of the requirements for the degree of

Bachelor of Science

Department of Physics and Astronomy

Brigham Young University

August 2015

BRIGHAM YOUNG UNIVERSITY

DEPARTMENT APPROVAL

of a senior thesis submitted by

Benjamin D. Smith

This thesis has been reviewed by the research advisor, research coordinator, and department chair and has been found to be satisfactory.

Date	R. Steven Turley, Advisor
Date	Eric Hintz, Research Coordinator
Date	Richard Vanfleet, Department Chair

ABSTRACT

Reflectance Measurements of Two Thin Film Materials in the UV

Benjamin D. Smith

Department of Physics and Astronomy

Bachelor of Science

The optical constants for yttrium oxide are presented for the 8.5-31 nm range. Y_2O_3 thin films have shown promise as a non-volatile reflector for EUV light at λ30.4 nm. Samples were prepared using e-beam vapor deposition and annealed at 800 K and 825 K. Optical constants were measured using reflectance methods at the Advanced Light Source. Measured values are compared to similar data taken in 2009 as well as calculations from the CXRO atomic scattering factors. I also present an experimental system to produce and measure the reflectance of aluminum films in the VUV range of 70-95 nm with applications in space-based astrophysical research. A hollow cathode He+ plasma discharge source was constructed and attached to a recommissioned monochromator and a variable-angle reflectometer. I provide some preliminary spectral and spatial characterizations of the UV light.

ACKNOWLEDGMENTS

My Father in Heaven - For loving me enough to let me struggle and have bad days occasionally, some of the most valuable lessons of my education; you patiently taught me that I have an intrinsic and unlimited worth, both as a person and as your son.

Dr. R. Steven Turley - For sharing your love of physics and enthusiasm for teaching during countless individual teaching moments; for supporting me in my research and even scrambling with me to complete this thesis until mere minutes before graduation.

Dr. David D. Allred - For being perceptive of my desires and goals and taking the time to listen to them.

Stephanie Thomas - For being a wonderful, loyal friend and even asking "What can I do to help you?" when truthfully you had no time to give; for willingly proofreading this document for me.

W. Scott Daniels - For instilling in me a deep fear and respect of high voltage; for your dry and sarcastic comments, ready smile and especially for teaching me about the power of the Atonement.

XUV Group Members: Kameron Hansen (ALS data analysis), James Adams (grating motor mover program), Joel Fuentes (grating stepper motor).

Jeremy Peterson and staff (machine shop); John Ellsworth, Tyler Westover and staff (vacuum systems and electronics).

This work was supported by the *BYU Department of Physics and Astronomy.*

Contents

List of Figures

Chapter 1

Introduction

1.1 Ultraviolet Light: Introduction and Applications

A recently active area of research has been the study of the region of the electromagnetic spectrum that lies between visible light and x-rays. We call photons with energy in this region *ultraviolet*. Wavelengths of light in the ultraviolet region extend from 400 nm down to about 5 nm (3.1 eV to 250 eV)[6]. The ultraviolet spectrum is commonly segmented into different divisions, given here by decreasing wavelength:

- UVA, from 400 nm to 315 nm, also called "black light";
- UVB, from 315 nm to 280 nm, with energies that are biologically hazardous;
- UVC, also called Vacuum Ultraviolet (VUV), from 280 nm to 40 nm, which is completely blocked by atmosphere;
- Extreme Ultraviolet (EUV), from 40 nm to 5 nm[1].

Figure 1.1 is a chart of the different divisions, showing the relative wavelengths and energies of each.

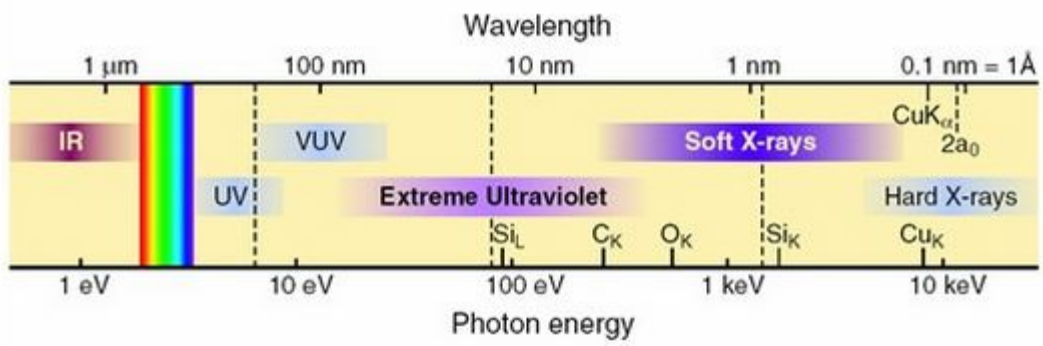

Figure 1.1: The electromagnetic spectrum containing the ultraviolet region[1]

The high-energy portion of ultraviolet (EUV and VUV) contains many atomic resonances as well as K- and L-absorption edges of many molecules and low and intermediate Z elements. This is extremely useful for precise chemical identification. Although many materials are completely transparent to visible and x-ray light, such as SiO_2, these atomic properties make them more strongly absorbent and more difficult to work with in the ultraviolet range[1].

1.1.1 IMAGE Mission

Interest in the EUV reflectance at BYU began back in the late 90s. NASA was completing and launching an orbiting satellite called Imager for Magnetopause-to-Aurora Global Exploration (IMAGE). The purpose of the mission was to take pictures of light from Earth's magnetosphere. The magnetosphere is an area of space surrounding our planet controlled by the its magnetic field[7]. Charged particles interact very strongly with the Earth's magnetosphere and give off light, sometimes as visible light, but often as EUV. Figure 1.2 is an EUV picture taken on the IMAGE mission of the Earth. You can see the bright ring of the Aurora Borealis that circles the North Pole. Of particular interest in this mission was the EUV light emitted by ionized helium atoms, having a wavelength of 30.4 nm[2]. We can learn a wealth of information

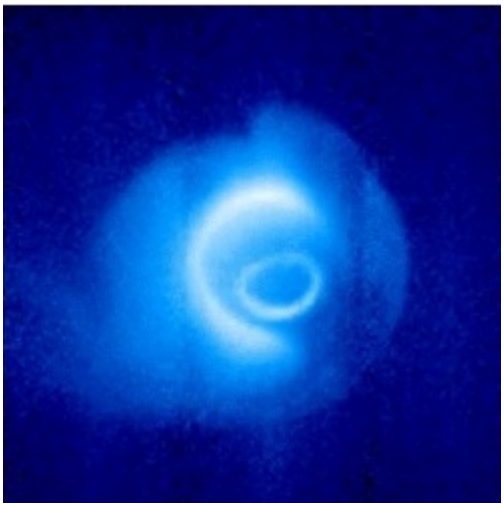

Figure 1.2: EUV image of Earth's Magnetosphere[2]

about our planet's magnetosphere and how it interacts with solar events from the EUV light emitted [8].

1.1.2 Additional Applications

The small wavelengths of EUV light makes it practical for imaging very small features on a surface. In the computer chip industry, the component feature size that manufacturers can produce is limited by the wavelength of light in their photolithography processes. EUV light at 13.5 nm has the potential to push the feature size all the way down to near the quantum limit, yielding faster, smaller, and more dense chips[9].

EUV and VUV light also have interesting applications in astrophysical research. Stars like our sun emit this kind of light from their super-hot, dense cores and from coronal mass ejections[10]. It is proposed that Lyman series radiation (91.2 nm to 121.6 nm) interacts with chemical compounds in our own galaxy and in the intergalactic medium[11]. High-energy ultraviolet light is showing significant promise in exoplanet research. The chemical fingerprints that this light provides can tell us about the composition and formation of exoplanet atmospheres[12].

The biological sciences also use this light for imaging cellular components and protein structures, with resolution and consistency previously unavailable from visible and electron microscopy[13]. All of these research areas require the accurate measurement and optical manipulation of high-energy ultraviolet light. For this reason, we are seeking to understand the optical properties of materials in this regime and learn how to produce better optical devices.

1.2 Purpose

There are two main aspects to this project:

1. *Experimentally determine the optical constants of* Y_2O_3: There were slight discrepancies between Muhlestein's 2009 data and the CXRO calculations for the optical constants. This repeated experiment will hopefully verify our previous measurements and confirm our sample preparation techniques.

2. *Develop and characterize an instrument capable of producing VUV light (70–95 nm)*: We eventually want to experimentally measure the reflectance of unoxidized evaporated aluminum metal films in the vicinity of its plasma edge. Our previous monochromator system employs a grazing-angle diffraction grating to disperse the light that is effective at shorter wavelengths. By recommissioning a near-normal incidence monochromator, we can get the light energies that we want. We also want to develop a stable, reliable, well-characterized VUV plasma discharge source to use in our reflectance measurements.

1.3 Previous Work: Yttrium Oxide

1.3.1 Shannon Lunt

Around the same time of the IMAGE mission, the Thin Films/EUV research group at BYU was tasked with designing and optimizing a mirror for this mission to reflect EUV light. In 1999, Shannon Lunt developed a genetic computer algorithm to predict which materials and layer configurations would yield good reflectance at 30.4 nm, the $2p \rightarrow 1s$ transition in He+ ions, and low reflectance at 58.4 nm, the $2p \rightarrow 1s$ transition in neutral helium [14]. Using the optical constants from the CXRO database, Shannon determined that the best candidate for an EUV reflector would be a multilayer stack of alternating Y_2O_3 and Aluminum. Y_2O_3 was also a good choice because the compound is already oxidized and very stable. Attempts to produce the mirrors to the theoretical specifications yielded lower reflectances than was predicted. Among other things, she cited "discrepancies in the optical constants" as a possible explanation for the reduced reflectances[14].

1.3.2 Joseph Muhlestein

Building off Lunt's work, undergraduate student Joseph Muhlestein experimentally measured the optical constants of Y_2O_3 in 2009. Thin films of Y_2O_3 were evaporated onto silicon substrates and reflectance tests over the range of 5–30 nm were carried out at the Advanced Light Source. Joseph's measured data was very similar to the CXRO data[3], but he eventually concluded that "significant difference, however, was shown to warrant the use of the experimentally determined index". Joseph's data analysis showed greater uncertainty at wavelengths above 25 nm[13]. His data is shown on a plot with the CXRO data in Figures 4.9 and 4.10. Joseph's samples were prepared using a electron-beam evaporator. We wanted to confirm that samples of

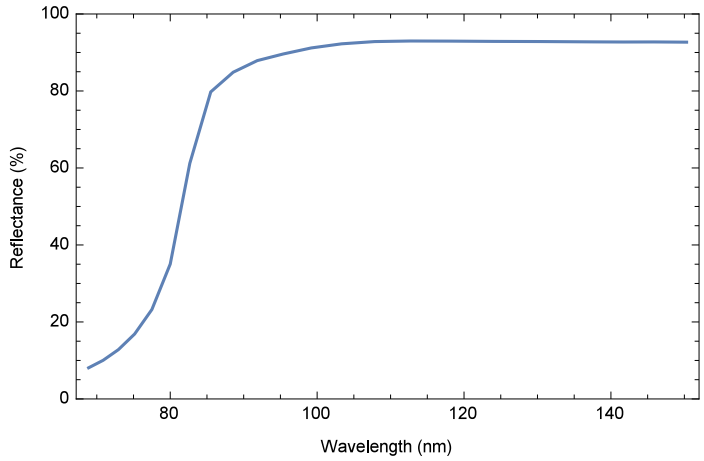

Figure 1.3: Reflectance of Aluminum from Kramers-Kronig analysis

Y_2O_3 prepared in a similar fashion produced equivilent reflectance data.

1.4 Previous Work: Aluminum

Optical constants of aluminum were tabulated in [15] based off a Kramer-Kronig analysis of data from [16] in the 100 nm to 32 μm range. This data gives the reflectance curve shown in Figure 1.3 . This indicates that aluminum may reflect well down to about 85 nm before becoming almost completely transparent. [17] showed that the reflectance of a freshly-deposited thin film of aluminum greatly decreases in the VUV when oxide begins to grow on the surface. Films were prepared in a vacuum environment with an O_2 partial pressure of 10^{-6} torr. Figure 1.4 shows how the reflectance of an aluminum film changes over time following deposition. The bottom curve shows the immediate drop in reflectance when O_2 was introduced to the system. The top curve is a control test with nitrogen gas. This data was taken with light at 121.6 nm. Madden et al. concluded that the reflectance of aluminum drops drastically in the VUV when covered with an oxide layer.

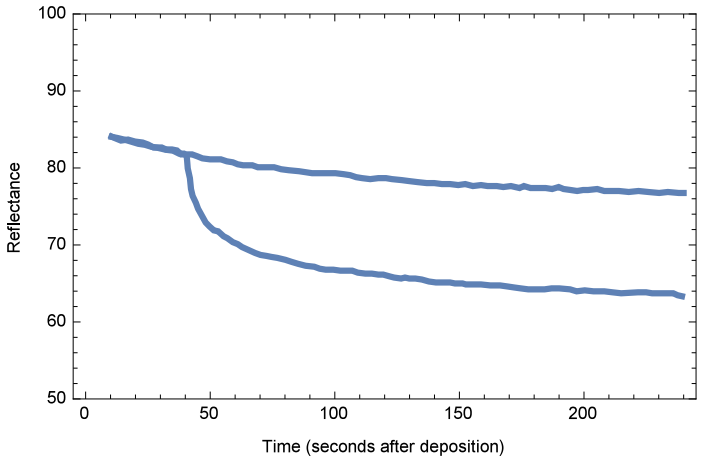

Figure 1.4: Reflectance change for an aluminum film with the introduction of nitrogen vs. oxygen.

1.5 Material Optics

1.5.1 Index of Refraction: Optical Constants

The optical constants for a particular material are complex numbers which uniquely characterize how light interacts with it. It is defined as:

$$\mathcal{N} = n + i\kappa. \tag{1.1}$$

The optical constants are the combination of what we call the 'real part' and the 'imaginary part'. The real part (commonly labeled n) describes how much light bends as it enters the material. The imaginary part (commonly labeled κ) describes how transparent a material is to light. We cannot directly measure the values of n and κ, but they can be calculated from reflection and transmission measurements. Both optical constants for a material depend on the frequency of light, or $n(\omega)$ and $\kappa(\omega)$.

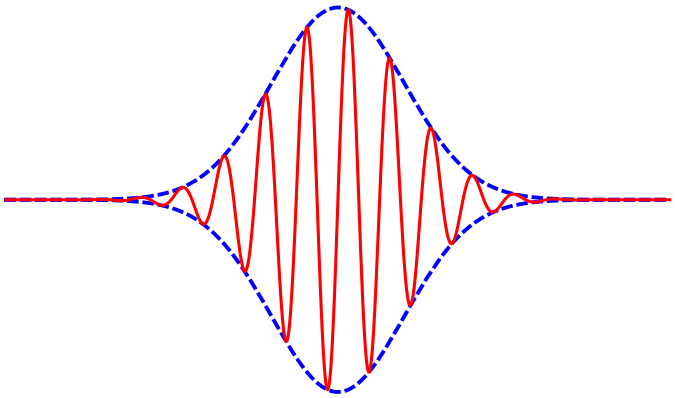

Figure 1.5: A wave packet of light

1.5.2 Optical Constants: The Real Part and Phase Velocity

The value n is responsible for light bending as it passes from one material into another. These properties can be used in a number of applications, from building microscopes and telescopes to non-glare eyeglasses.

In vacuum, light travels at a constant speed of $c = 2.998 \times 10^8$ m/s. Light waves can travel in packets, or pulses that propagate at the speed of light. Figure 1.5 shows that individual wave crests and troughs (the red lines) lie within the packet envelope (the blue dashed lines). These 'wiggles', however, can actually move either faster or slower than the overall packet relative to the center. The speed of the wiggles that are contained within the packet is called the phase velocity v_p. In the limit that the pulse is very long, we can approximate the light as a plane wave.

We define the index of refraction as the direct ratio between the speed of light in a vacuum to phase velocity in the material. In other words, $\mathcal{N} = \frac{c}{v_p}$. The phase velocity of light increases marginally for certain materials in the x-ray and extreme ultraviolet region. These materials have an index of refraction slightly less than one[18].

1.5.3 Optical Constants: The Imaginary Part

The imaginary part of the complex index of refraction κ quantifies the transparency of a material. In most transparent materials, κ is very close to zero and almost negligible, however, it increases for materials with greater opacity. As light enters a material, the wave begins to decrease in amplitude. The amplitude of the wave decays exponentially through the material, as depicted in Figure 6. κ quantifies how quickly the wave dies off; a higher value leads to faster decay. For this purpose, κ is often called the "extinction coefficient".

Here I will demonstrate how κ is responsible for the decay of a wave[19]. A plane wave for an oscillating electric field traveling along the x-direction inside a material can be represented as

$$E(x,t) = E_0 e^{i(kx-\omega t)}. \tag{1.2}$$

k is the magnitude of the wavevector and in vacuum it has the value

$$k = \frac{\omega}{c} = \frac{2\pi}{\lambda}. \tag{1.3}$$

In a material,

$$k = \frac{\mathcal{N}\omega}{c} = \frac{(n+i\kappa)\omega}{c}. \tag{1.4}$$

Substituting this value of k into equation 1.2 gives

$$E(x,t) = E_0 e^{i(\frac{(n+i\kappa)\omega}{c}x-\omega t)} \tag{1.5}$$

Separating terms and simplifying

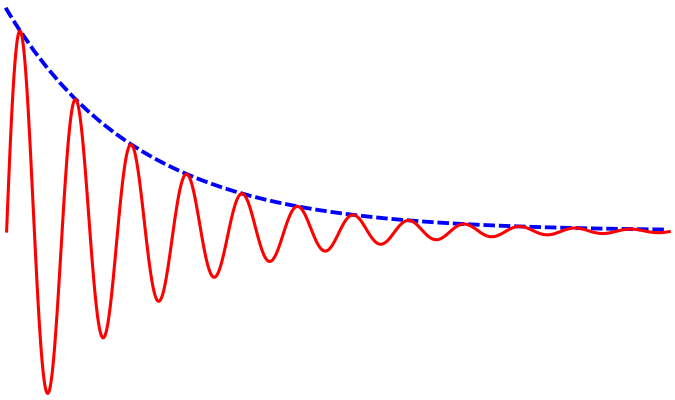

Figure 1.6: The exponential decay of a wave scaled with κ

$$E(x,t) = E_0 e^{i(\frac{n\omega}{c}x - \omega t)} e^{-\frac{\kappa\omega}{c}x} \tag{1.6}$$

The first term is the oscillation part and the second represents a decaying exponential. The product of the two terms represents the function of a wave that decays as shown in Figure 1.6 .

1.6 EUV Optics and Thin Films

1.6.1 Light Reflectance From a Single Surface

In the 1800s, Augustin Fresnel determined that the percentage of light reflected $\mathcal{R}$, or the reflectance, depends on the incidence angle and transmittance angle of the light relative to normal incidence, θ_i and θ_t, and the indices of refraction of the two materials at the interface, $\mathcal{N}_1$ and $\mathcal{N}_2$. This is shown in Figure 1.7 . The angles and indices are related by Snell's law:

$$\mathcal{N}_1 \sin\theta = \mathcal{N}_2 \sin\theta_t. \tag{1.7}$$

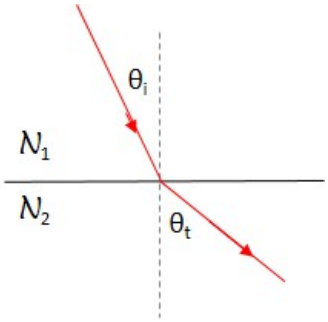

Figure 1.7: Refraction at an interface

The Fresnel coefficients for reflection differ depending on the polarization of the light, whether it is polarized parallel to the surface (s) or parallel to the plane of incidence (p). These coefficients[19] are:

$$r_s = \frac{\mathcal{N}_1 \cos\theta_i - \mathcal{N}_2 \cos\theta_t}{\mathcal{N}_1 \cos\theta_i + \mathcal{N}_2 \cos\theta} \tag{1.8}$$

$$r_s = \frac{\mathcal{N}_1 \cos\theta_t - \mathcal{N}_2 \cos\theta_i}{\mathcal{N}_1 \cos\theta_t + \mathcal{N}_2 \cos\theta_i}, \tag{1.9}$$

and the reflectances for each polarization are

$$\mathcal{R}_s = |r_s|^2 \tag{1.10}$$

$$\mathcal{R}_p = |r_p|^2 . \tag{1.11}$$

Notice that near normal incidence (i.e. $\theta_i = \theta_t = 0$) we see that

$$\mathcal{R} = |r_s|^2 = |r_p|^2 = \left|\frac{\mathcal{N}_1 - \mathcal{N}_2}{\mathcal{N}_1 + \mathcal{N}_2}\right|^2 . \tag{1.12}$$

Knowing the fractions of s- and p-polarized light (f_s and $f_p = 1 - f_s$, respectively), the total reflectance of light from a material is defined as

$$\mathcal{R}_{tot} = f_s\mathcal{R}_s + (1 - f_s)\mathcal{R}_p. \tag{1.13}$$

1.6.2 Multilayer Thin Films and Interference

Most solid materials have a v_p in the EUV that is just slightly higher than c, giving an $\mathcal{N}$ that is less than, but very close to one[1]. This means that light won't refract very much as it enters the material. We can also see from Equation 1.12 that if $\mathcal{N}_1$ and $\mathcal{N}_2$ are close to each other, then $\mathcal{R}$ is approximately 0. For materials in the EUV, κ is typically non-zero but significant enough to attenuate the light as it passes through. This attenuation makes bulk materials poor EUV reflectors. We can, however, achieve greater reflectances by using thin film multilayer stacks.

In Newton's *Opticks*, he described his observations with light reflecting off the films of soap bubbles. He observed that there were places on the bubble surface that reflected different colors, giving it an iridescent sheen. There were even some places where no light at all was reflected and appeared as dark black regions. He noticed that these regions of colors changed as the bubble film evaporated into the air. From his observations, Newton concluded that the thickness of the bubble film affects how light reflects off it[20].

When a layered material, like a soap bubble has two or more interfaces, called a multilayer stack, we can see these interference effects at play. Light reflects off each interface as it passes through the multilayer, as shown in Figure 1.8 . The phase velocity v_p inside the film material $\mathcal{N}_2$ is different than in the first material $\mathcal{N}_1$. The wave fronts for the reflected light from the top and bottom surface recombine, the light from the bottom surface having traveled a longer distance inside the film. This causes one wave to be shifted in phase relative to the other. If the two waves are in phase, the electric fields combine together and they interfere constructively,

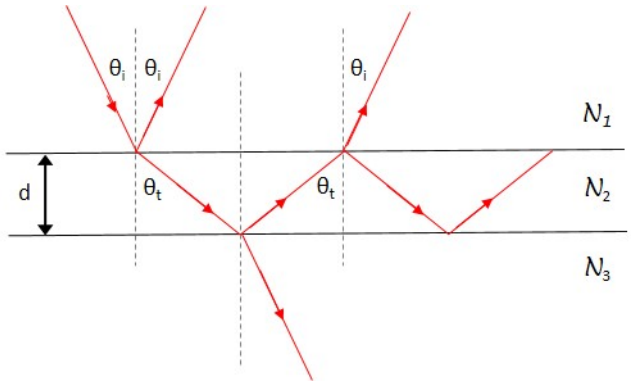

Figure 1.8: Thin film interference using ray tracing

yielding increased reflectance. If the the two waves are out of phase, then the electric fields partially cancel each other out and interfere destructively, yielding decreased reflectance. They cannot destructively interfere completely; the light that passes through the film is attenuated by κ, so it will have a different amplitude when it exits. Interference from a thin film depends the optical path length inside the film; it also depends on the index of the materials at the lower interfaces. A 180° phase change occurs if $\mathcal{N}_3 > \mathcal{N}_2$. No phase change occurs if $\mathcal{N}_3 < \mathcal{N}_2$. For a single film, the condition for constructive interference is summarized as

$$2\mathcal{N}_2 d\cos\theta_t = m\lambda \qquad \text{(No phase change)} \tag{1.14}$$

$$2\mathcal{N}_2 d\cos\theta_t = (m+\frac{1}{2})\lambda \qquad \text{(Phase change)} \tag{1.15}$$

where d is the thickness of the film, λ is the wavelength of light, and m is an integer $m = 1, 2, 3...$ The interference also depends on the complex angle θ_t of the light inside the material (remember that θ_t is related to θ_i by Snell's Law, Equation 1.7). If the angle is larger, then the optical path length inside the film is greater. In our measurements, we record the intensity of reflected light as a function of incidence

angle. In our data sets we observe sudden dips in the reflectance curve, as shown in Figure 3.1. These dips or interference fringes at various angles are caused by the destructive interference of the light reflected off top and lower interfaces.

1.6.3 The Parratt Multilayer Formula

We calculate reflectances of multilayer stacks using a modified version of the Fresnel coefficients and a recursive formula developed by Parratt [21]. The reflected amplitude of light in a single layer $R_1^{'}$ is used to calculate the the reflected amplitude in the next layer above it $R_2^{'}$, and so on. This formula applies equally to s- and p-polarizations. It is given as

$$R_2^{'} = \frac{C(r_{21} + R_1^{'})}{1 + r_{21}R_1^{'}}, \tag{1.16}$$

where the Fresnel coefficients

$$r_{21}^{s} = \frac{k_{z2} - k_{z1}}{k_{z1} + k_{z2}} \tag{1.17}$$

$$r_{21}^{p} = \frac{\mathcal{N}_1^2 k_{z2} - \mathcal{N}_2^2 k_{z2}}{\mathcal{N}_2^2 k_{z1} + \mathcal{N}_1^2 k_{z2}} \tag{1.18}$$

are now defined in terms of the z-components of the wavevector k (normal to the surface) and the real part of the indices of refraction of the two materials. The factor C is defined as

$$C = e^{\frac{ik_z d}{2}}, \tag{1.19}$$

and accounts for the phase shift that the electric field experiences as it passes through a film of thickness d. Inside the substrate layer, all of the light proceeds unreflected,

making $R = 0$ for this layer. From there, you can apply the formula to calculate the reflected amplitude inside each subsequent layer from the substrate. The thickness of the vacuum layer is taken to be zero. Before calculating the total reflectance amplitude inside the vacuum R'_{vac}, we take into account the possible roughness of the top surface. Non-planar deviations on the surface can scatter light in non-specular directions and manifests itself as decreased reflectance. We multiply the reflectance amplitude inside the top layer R'_{top} by the corrective factor

$$s = e^{-\frac{q^2\sigma^2}{2}}, \tag{1.20}$$

where $q = \frac{2\pi}{\lambda}\sin(\theta)$ and σ is the root mean squared (RMS) roughenss. The term s is called the Debye-Waller factor.

If we assume that our roughness is periodic, then we can represent it as the sum of periodic sine and cosine functions. This factor s assumes a Gaussian distribution of spatially periodic "waves"[18, 13]. It could similarly be applied at each interface in the recursion formula, but for our purposes we just assume a top surface roughness.

The total reflectance $\mathcal{R}$ can now be calculated from the reflectance amplitude inside the vacuum.

$$\mathcal{R} = \left|R'_{vac}\right|^2. \tag{1.21}$$

The Parratt recursion formula together with the Debye-Waller factor are contained in the function `parrattRough` in the **refl.m** class in A.1.

1.6.4 Optical Constant Convention

Many who study the optical properties of materials in the EUV use a slightly different convention in referring to the optical constants. Because n is less than, but very close

to 1, they instead use the value of δ, where $n = 1-\delta$. Also the value κ is interchanged for β to distinguish it from value k, the magnitude of the wavevector. The complex index of refraction is then expressed as

$$\mathscr{N} = 1 - \delta + i\beta. \tag{1.22}$$

In order to be consistent with the literature, I will employ this convention throughout the remainder of this paper.

1.7 The Independent Atom Approximation

The independent atom approximation is a theoretical model for calculating the optical constants for every material at all wavelengths. This model allows one to calculate the optical constants by only knowing the chemical compounds of the material and the density of those atoms in the material.

The optical constants are calculated from the atomic scattering factors, which are a measure of how well a given atom scatters light for a particular wavelength. The basic assumption of this approximation is that we can model the atoms in a material as light-scattering bodies which don't interact with each other [3]. Generally, this is a good approximation provided that we are not near any atomic absorption resonances. This approximation breaks down at longer wavelengths, where we have fewer core electrons partcipating in the interaction.

1.7.1 Atomic Scattering Factors

Atoms, electrons and other particles have the ability to scatter light in different directions[1]; this effect is responsible for the blue color of the sky and the twinkling of stars. Specifically, an atom's ability to scatter light is the sum of the scattering by

each of its bound electrons. This sum is called the atomic scattering factor or f^0. To find this factor for a particular atomic species, we can employ a semi-classical driven harmonic oscillator model of the electrons in an oscillating electric field[5]. A more complete derivation is provided in Appendix B, but I will cite the results here.

The atomic scattering factor f^0 is a complex number

$$f^0(\omega) = f_1^0(\omega) - if_2^0(\omega). \tag{1.23}$$

and is related to the index of refraction by[18]

$$\mathcal{N}(\omega) = 1 - \delta(\omega) + i\beta(\omega) = 1 - \frac{N_a r_0 \lambda^2}{2\pi}(f_1^0 - if_2^0). \tag{1.24}$$

Here, N_a is the atomic density of the material, r_0 is the classical electron radius (2.81794×10^{-15}m) and λ is the wavelength of light.

1.7.2 CXRO Data

The Center for X-ray Optics (CXRO) at Lawrence-Berkeley National Lab is a frequently-referenced assembly of material optical data in EUV and x-rays. They have created a database of these optical constant calculations for all materials and layer configurations in the EUV/X-ray regime[3]. Their optical data is computed from the independent atom approximation. While the independent atom approximation is a very powerful model in its predictive ability for optical constants, it does have limitations. It makes the relatively poor assumption that the atoms that make up a material interact only with the light. In reality, there are many interactions taking place inside a material, specifically between atoms themselves. The model is unable to takes these factors into consideration. Calculations of optical constants from CXRO are often close to measured values, but significant and noticeable deviations appear particu-

larly at longer wavelengths; this is where the light waves involved in the calculations are less localized on single atoms [14].

Their calculations are taken from the atomic scattering factors specific to each element. For a chemical compound, the values of δ and β are simply the weighted average of the optical constants for the individual elements[13]. They are weighted by the relative densities of each element in the compound. In the case of Y_2O_3, where there are 2 yttrium atoms and 3 oxygen atoms:

$$\delta_{Y_2O_3} = 2\frac{\rho_{Y_2O_3}}{\rho_Y}\delta_Y + 3\frac{\rho_{Y_2O_3}}{\rho_O}\delta_O \tag{1.25}$$

$$\beta_{Y_2O_3} = 2 \cdot \frac{\rho_{Y_2O_3}}{\rho_Y}\beta_Y + 3\frac{\rho_{Y_2O_3}}{\rho_O}\beta_O \tag{1.26}$$

1.8 Reflectance of Aluminum

Metal aluminum shows promise for applications in space-based VUV telescopes. It works very well as a broadband, first-surface mirror for wavelengths all the way down to 85 nm.

I showed in section 1.7.1 that materials like Y_2O_3 reflect light because electrons in the material respond to and re-scatter the oscillating electric field of incoming light. Electrons in materials that are mostly bound to the atomic nuclei obey the equation of motion Equation B.1. A distinguishing feature of this equation is the third term on the left side, $m\omega_s x$, called the restoring term.

Metals such as aluminum are electrically distinct from materials like Y_2O_3. Instead of every electron being bound to its nucleus, the upper-level valence electrons are free to travel throughout the material and are shared by all the nuclei in the material. The clouds of valence electrons on the surface are responsible for light reflection; for

this reason, metal reflectors like aluminum are called first-surface mirrors.

Since the electrons are free to move and there are an equal number of opposite charges in a neutral metal, we can treat the material as if it were a plasma. Neutral plasmas have the property that they reflect light well at low frequencies and are completely transparent at high frequencies. A good example of this is the ionosphere, a low-altitude portion of Earth's magnetosphere. Radio waves can bounce off this layer, but visible photons pass through unimpeded. The frequency where this transition occurs from reflecting to transmitting is called the plasma frequency. A further derivation and discussion of the plasma frequency is provided in Appendix C.

The plasma frequency of pure aluminum metal has been calculated and measured using the Drude model and has a corresponding wavelength around 85 nm[15] as shown in Figure 1.3, although other estimates place it even lower at 78 nm[22]. Aluminum has the property that its surface oxidizes very rapidly due to oxygen in the air. Oxygen is a highly electronegative element and therefore attracts the free valence electrons of aluminum. The oxygen ions bind to the metal surface creating the a film of aluminum oxide. Al_2O_3has very different reflective properties than the pure metal. It's reflectance drops dramatically in the ultraviolet with the introduction of this oxide layer.

1.9 Light Generation

In this section, I will describe two sources of UV light that we use in our measurments: synchrotron radiation and light from a hollow cathode plasma discharge source.

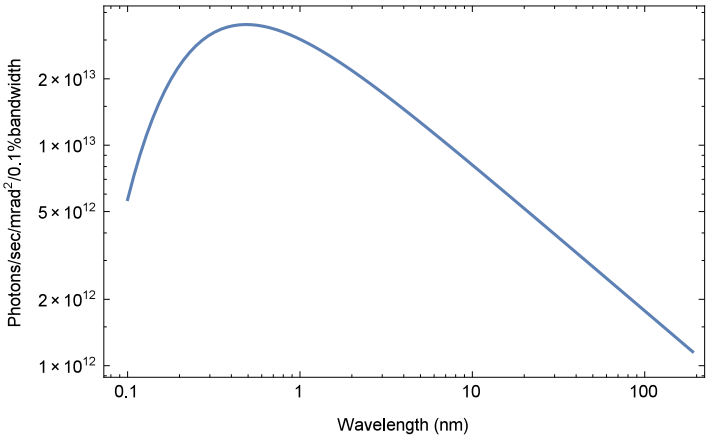

Figure 1.9: Spectrum of the ALS[3]

1.9.1 Synchrotron Radiation (ALS)

Synchrotron radiation is the light emitted by relativistic electrons when they are accelerated in a magnetic field. The electrons produce a narrow cone of radiation that propagates tangential to their path. This gives the appearance of a searchlight sweeping around the bend. The Advanced Light Source (ALS) at Lawrence-Berkeley National Lab in Berkeley, CA houses a third-generation synchrotron optimized for ultraviolet and X-ray research[23]. The electrons in the storage ring have an energy of 1.90 GeV and produce a current of about 500 mA. The bend magnet has a field strength of 1.27 T[1, 3]. Synchrotron radiation produces a broadband spectrum instead of discrete transition lines. The spectral brightness of the ALS is shown in Figure 1.9 . The spectral brightness is the photon flux per unit area and per unit solid angle and per unit unit relative spectral bandwidth[1].

The ALS and the beamline on which we take data have the benefit of being finely-tuned and calibrated systems. The spectrum is optimized for working in the EUV range, but lower by about a factor of 10 in the VUV 70-110 nm range. Since the ALS is also a considerable distance away, we can only take stable, non-volatile samples there for measurements, such as Y_2O_3. Taking freshly grown aluminum film samples

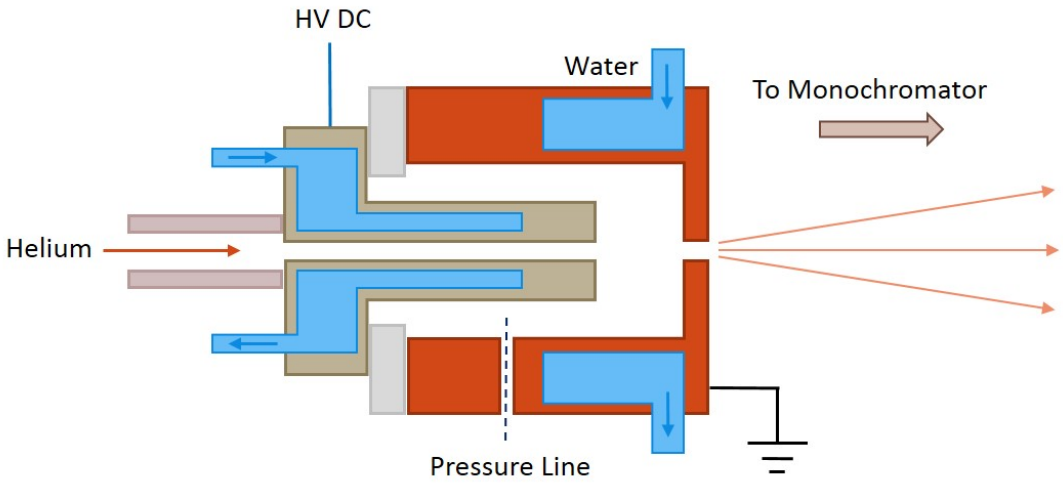

Figure 1.10: Diagram of Hollow Cathode Source

to the ALS for measurements without them oxidizing is a practical impossibility.

1.9.2 Hollow Cathode Discharge Source

A hollow cathode source is a device that produces UV, EUV and X-ray light through collisions between atoms, ions, and electrons. It has many applications, particularly in photolithography [9]. In this device, gas flows into in a cavity that contains a grounded anode and a high negatively-charged cathode. The gas is typically an inert noble gas. The high electric field inside the device has the potential to ionize some of the gas molecules, creating a plasma of free electrons and positively charged ions. The electron, because of its low mass, is quickly accelerated in the direction of the anode and the massive ion proceeds more slowly in the opposite direction towards the cathode. Figure 1.10 is a cross-sectional diagram of our hollow cathode source. The grounded anode is shown in burgundy and the cathode is the gray piece. An insulating spacer disk, shown in light grey, separates the cathode and anode so that current flows through the plasma.

Our hollow cathode is a cylindrical stainless steel piece with a gas line bored

through the center axis. There are cavities manufactured inside the piece and water can flow through them to keep the cathode cool. Water also cycles through the grounded anode. Our hollow cathode was recently redesigned with a thicker front metal surface between the internal water cooling and the external vacuum. Sputtering degrades this surface over time and there have previously been water leaks in the vacuum system as a result.

Much of the light from hollow cathode plasmas come from atom/ion-electron interactions. Accelerated electrons can transfer their energy to atoms and ions through physical collisions. These can impart enough energy to the bound electrons to induce transitions between energy levels. These produce light with specific, discrete transition lines. When an atom becomes ionized, its electrons are more tightly bound to the nucleus. Therefore, transitions between ionized energy states generally emit photons with higher energy. In addition, energetic electrons that pass near the vicinity of an ion can be accelerated and radiate broadband Bremsstrahlung[1].

We can characterize the plasma in terms of its mean free path, l. This is defined as the average distance between binary particle collisions. On average, an electron can acquire kinetic energy for a distance up to l before losing it to another collision. l depends on some of the physical properties of the plasma, primarily the temperature T, the ion density n_i, and the the average charge state $+Ze$. In summary,

$$l \propto \frac{(k_B T)^2}{n_i Z} \tag{1.27}$$

For our helium plasma, we estimated a mean free path of about 1 cm.

The stability and energy of the plasma depends on three separate parameters: the voltage, the current and the pressure. The voltage relates to the kinetic energy that an accelerating electron acquires between collisions. The radiated power and intensity of the light relate to both the current and the number of particles we have

in the plasma. The mean free path is inversely proportional to the pressure of the gas; as the pressure decreases, there is more space between individual particles and l increases.

There are trade-offs between these parameters. As the pressure decreases, l increases, leading to more energetic collisions. These collisions produce the kind of ultraviolet light that we use in our measurements. However, as the pressure decreases, the number of radiating particles in the plasma decreases also, thereby reducing the plasma's intensity. Also, we can only increase the current so high before our components begin to heat up dangerously.

The hollow cathode has the benefit of being small, cheap to operate and easily mountable on our monochromator. This is convenient for research conducted at BYU, especially for measuring samples *in situ*. We can use different types of noble gases to produce the desired bright transition lines.

Chapter 2

Data Acquisition

2.1 Yttrium Oxide

2.1.1 Description of System

We took our reflectance data at Beamline 6.2.3 of the ALS. This system was developed for the Center of X-ray Optics by Erik Gullikson in 1996[4]. Figure 2.1 shows the schematic of the beamline that we conducted our measurements on. The beam has an angular divergence of 1.85 and 0.44 milliradians in the horizontal and vertical directions respectively. The diameter of the photodetector is large compared to that of beam, so we have sufficient angular resolution from the detector. The monochromator has three remotely-interchangeable diffraction gratings of 300, 600 and 1200 lines/mm.

The reflectometer is a cylindrical vacuum chamber in the beamline wherein samples are tested. Monochromatic EUV light enters the chamber from a small opening on the side and reflects off the samples on the holder. The sample holder is a stage placed in the center of the chamber that rotates an angle θ around the chamber axis. This sample holder also contains motors which move the sample plate with 10 μm positional accuracy. The light detectors are mounted on an arm that pivots an angle

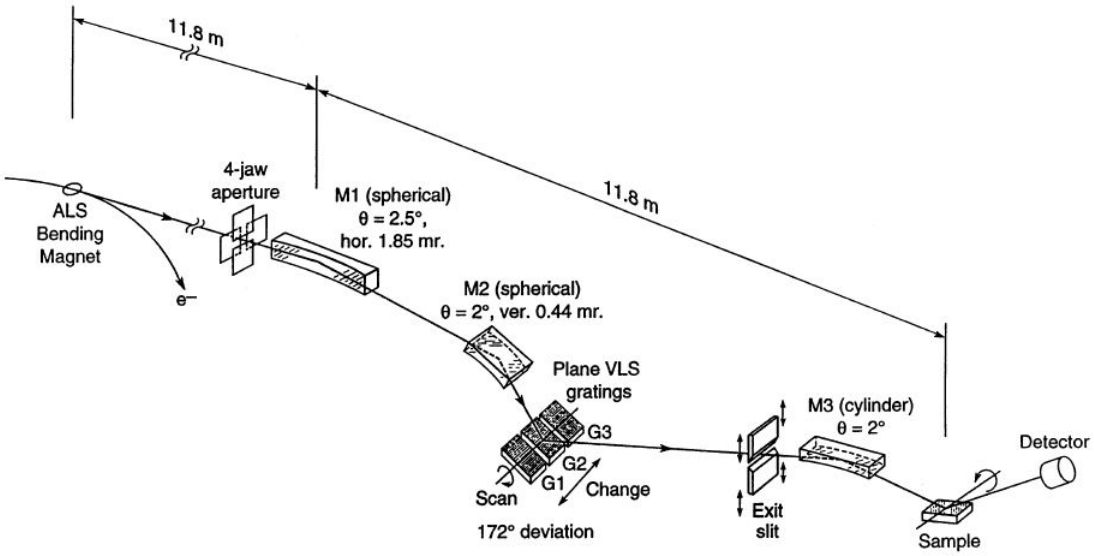

Figure 2.1: A schematic of Beamline 6.3.2 at the ALS[4]

ϕ around the axis of the chamber; for specular reflection measurements, $\theta = 2\phi$. The arm contains a phosphor window with a visible CCD camera behind. The phosphor down-converts the EUV light into visible photons and is used mainly for alignment purposes. An inwardly-oriented photodiode directly detects the intensity of the reflected EUV light. A gain amplifier circuit multiplies the photodiode signal by a factor of 10^G, where G is the gain. G takes integer values from 7–11.

2.1.2 Sample Preparation

David Allred and John Ellsworth prepared our sample with the electron beam evaporation unit at BYU. In this device, a silicon substrate with a thin silicon oxide film is inverted over a carbon crucible and the chamber is evacuated to 10^{-6} torr. The crucible contains solid chunks of Y_2O_3. A high-energy beam of electrons is emitted horizontally from underneath the crucible. A magnetic field curves the electron beam in a 270° self-focusing arc onto the chunks, thereby transferring kinetic energy into

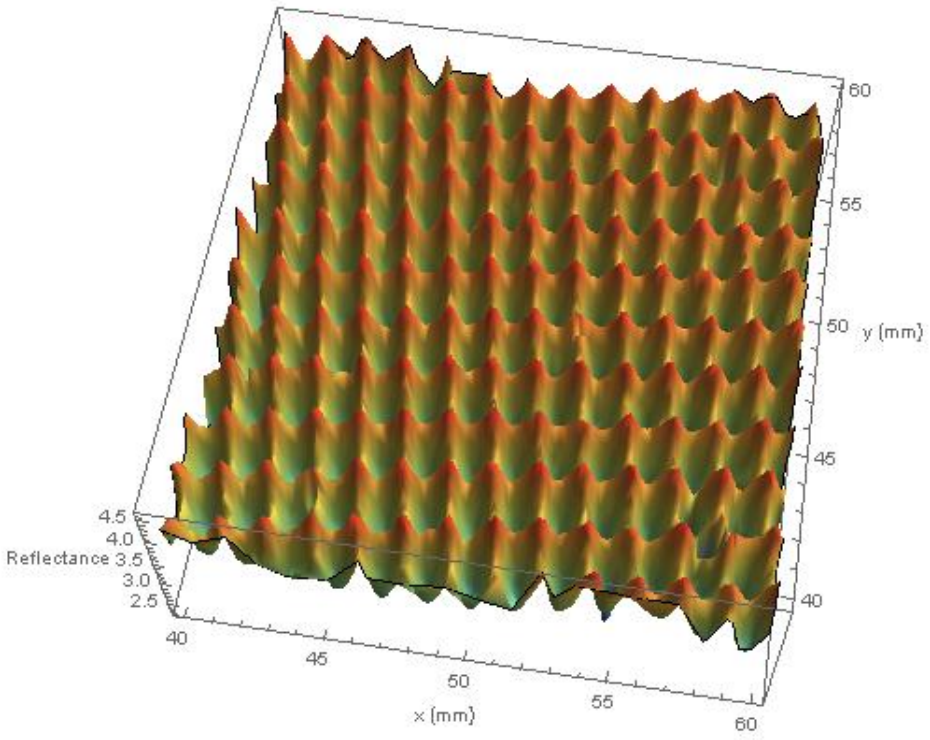

Figure 2.2: Periodic surface deviations on the sample

the Y_2O_3. Once a molecule has enough thermal energy, it is physically ejected upwards from the crucible and sticks to the substrate. After a short time, a thin layer covers the entire surface.

The e-beam device had previously been under repair and was not yet at full functionality. Allred and Ellsworth had no control over the beam current, which, they reported, was significantly higher than desired. The increased current caused entire flakes of Y_2O_3 to float out of the crucible and stick to the substrate. To reduce the number of flakes, Allred and Ellsworth placed a copper mesh of grid spacing 1.41×1.95 mm between the crucible and the sample. While this may have increased the overall uniformity of the sample, we later observed an image of the screen on one of the samples during our reflectance measurements. Figure 2.2 shows an XY

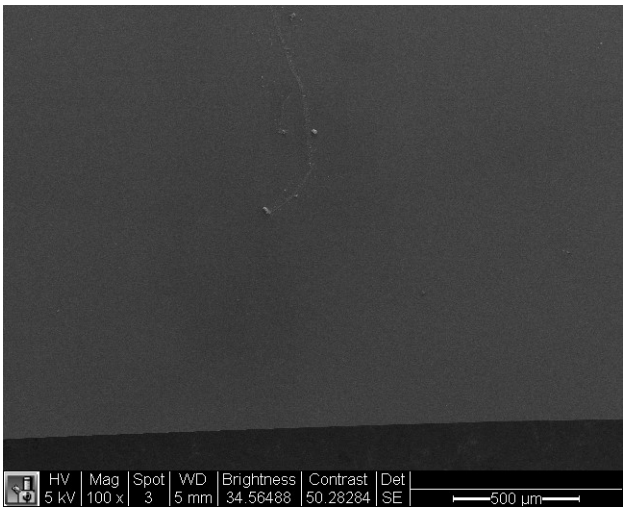

Figure 2.3: SEM image of our sample

reflectance scan of the surface of our sample. A periodicity of about 1.2 mm is clearly observable on the surface.

Following this first evaporation, another layer was evaporated on top of the first, the sample was annealed at 800 K for 20 hours. The annealing process removes any impurities in the sample.

2.1.3 Sample Characterization

After the samples were prepared and annealed, Allred used ellipsometry to conclude that the approximate thickness of the Y_2O_3 film was about 17 nm.

Stephanie Thomas and Paul Minson marked the approximate measurement position on the sample with an etching pen and imaged the sample with the SEM. Figure 2.3 is a 100x image of the scratch they made and the measurement site. They ran a top-down EDX scan to determine the elemental composition of the sample. The results of their scan are shown in Figure 2.4 . According to the EDX device, the sample consisted of silicon, yttrium, oxygen, and carbon. Thomas cited the SEM itself as a possible source of carbon contaminants. The sample was too thin to perform a

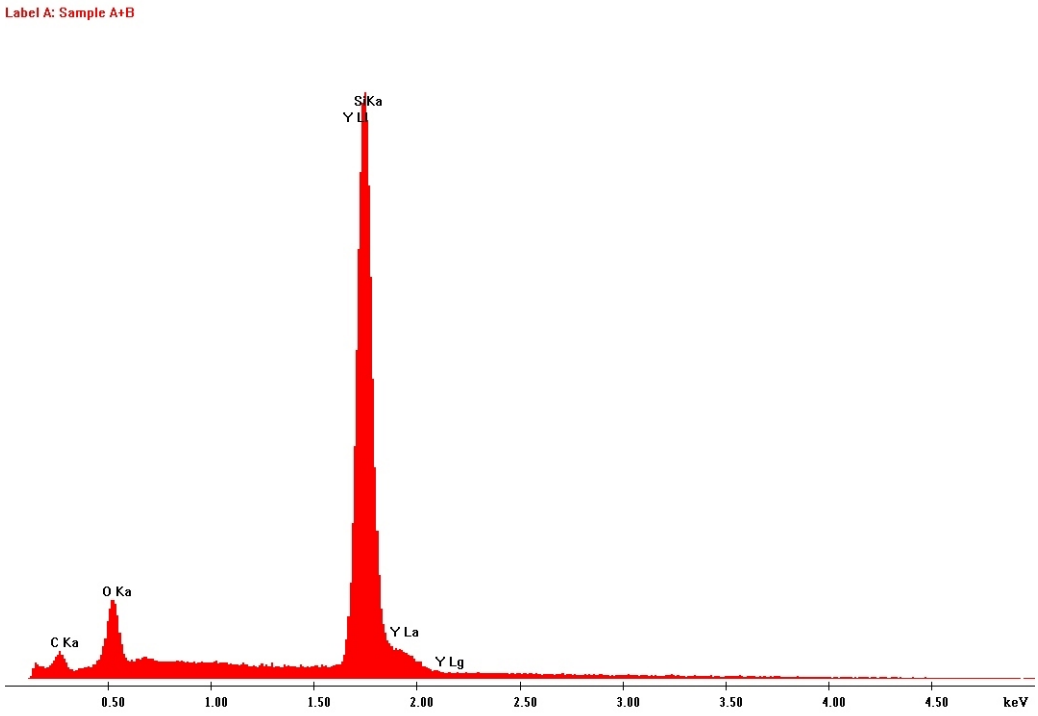

Figure 2.4: EDX scan of the sample

cross-sectional area scan.

Following these measurements, Allred used the AFM to physically measure the roughness of the sample's surface. Figure 2.5 shows a 1 μm x 1 μm scan where the RMS roughness was determined to be 0.173 nm. This RMS roughness is the same as the σ in the Debye-Waller factor. Figure 2.6 shows a power spectral density of the surface. Allred was confident that the sample was indeed smooth at the resolution of the AFM tip. If the sample were rougher, we would have seen the power spectral density histogram curve up on the right side.

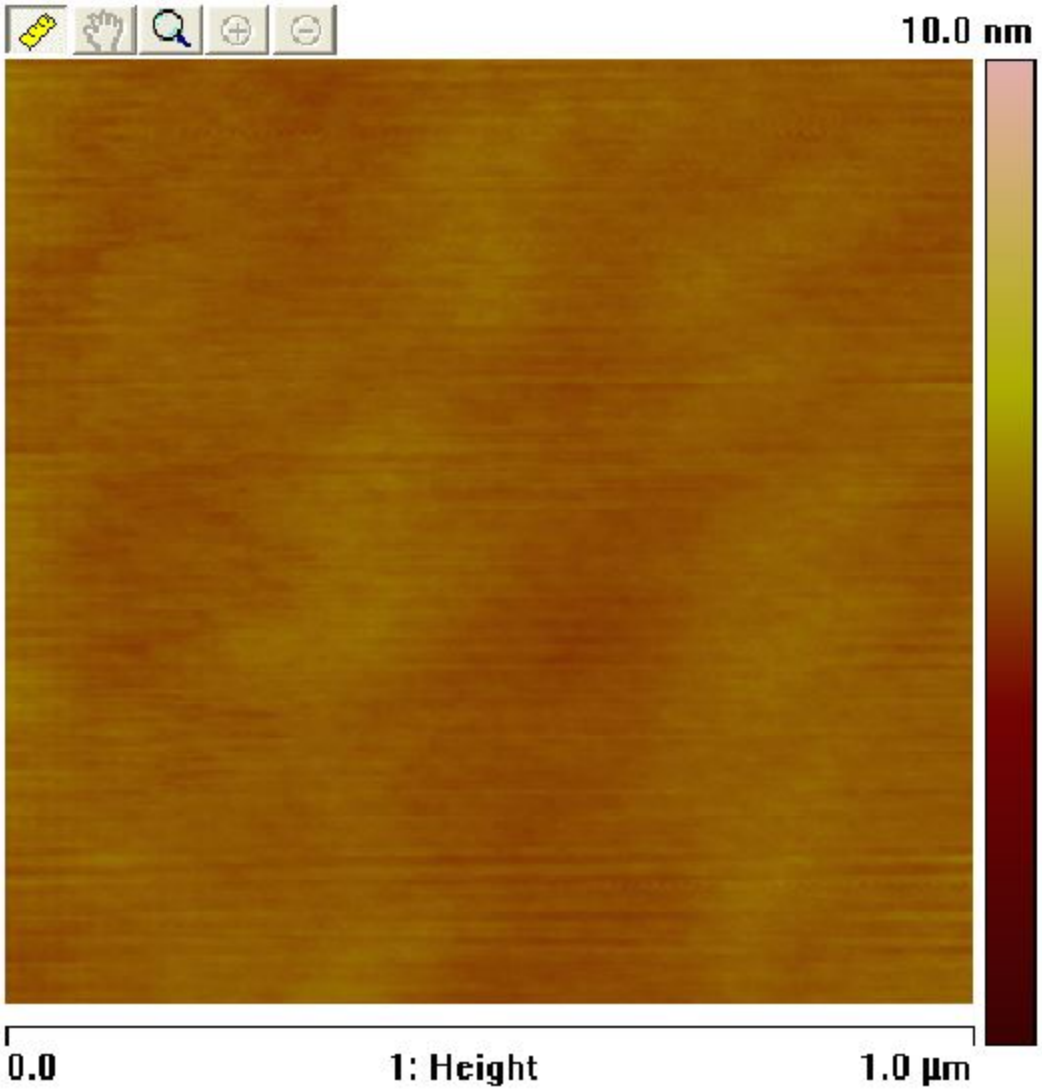

Figure 2.5: $1\mu m$ x $1\mu m$ AFM scan of our sample

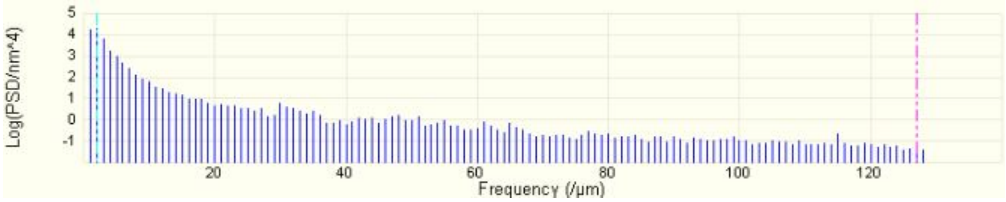

Figure 2.6: Power Spectral Density of the surface

2.1.4 Procedure

Alignment

Following a 30 minute pump-down, the sample holder was oriented relatively face-upwards and then lowered beneath the horizontal light beam. We scanned ϕ, using the phosphor detector to visually locate the beam. The angle at which the spot on the phosphor was brightest we assigned to $\phi = 0$.

The next step involved finding the zeroed height (z) and angle (θ) placement of the sample. If the sample is not at the correct initial height and angle, then the beam spot will move across the sample and measure different physical locations as θ increases. The phosphor detector was placed opposite of the beam at $\phi = 0$. We then followed an iterative process to place the sample flat (relative to the beam) and halfway into the beam itself.

1. Raise the sample holder in z until the phosphor intensity reduces by $\frac{1}{2}$ of the straight-through intensity.

2. Since one edge of the sample could be higher than the other, rotate the sample holder back and forth in θ until the phosphor intensity reaches its maximum.

3. Repeat 1 and 2 until no further improvements can be made. Assign that height to $z = 0$ and that angle to $\theta = 0$.

Once this alignment is complete, we have to find a smooth point on the sample to measure. Small deviations in the surface like roughness can compromise the reliability of our reflectance measurements. We set the grating to give light at 13 nm, a wavelength that this beamline produces well and one that is intermediate in our wavelength range. The sample holder is angled close to normal incidence relative to the beam; the detector is moved to twice that angle. We first made a scan of the

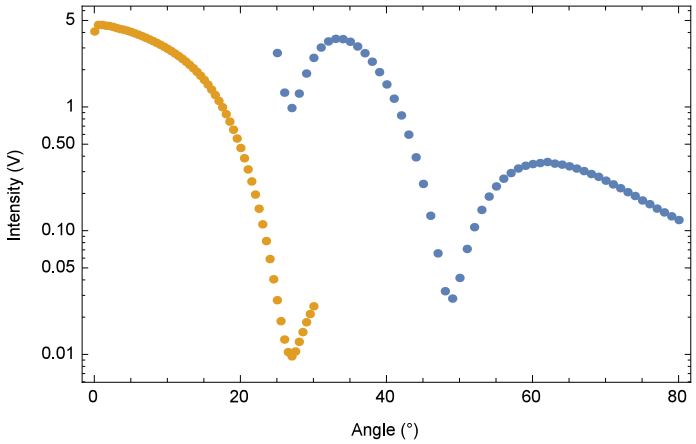

Figure 2.7: Segments of a $\theta/2\theta$ scan for λ12.5 nm, $G = 7$ (yellow) and $G = 9$ (blue)

sample by translating it in the x-direction and then noting the position on the sample where the reflectance didn't change significantly. We moved the sample to that x position and then repeated the scan, this time in the y-direction. By iterating between the two directions, we were able to find a site on our sample that was sufficiently smooth.

Scans and Data Parameters

A reflectance scan, or a $\theta/2\theta$ scan records the intensity of reflected light for a particular wavelength λ' as a function of θ, the angle of the sample holder relative to the beam from grazing incidence. We call it $\theta/2\theta$ because in order to collect the reflected light, the detector has to rotate by twice the angle that the sample holder rotates. For notational simplify, I will refer to this type of data as reflectance or $R(\theta)$. It was not possible to take one single scan over all angles from 0° to 80°. At larger angles, the signal eventually becomes so small that it is impossible for the computer to accurately read it. We composed a full scans from angular segments that each kept the signal in the 0.01 - 10 V range, each at different gain values G. Figure 2.7 shows two segments of a reflectance scan with light wavelength of 12.5 nm. The yellow plot

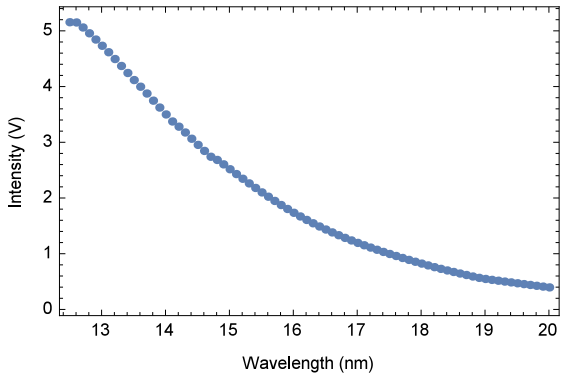

Figure 2.8: A typical i_0 scan, read with a G of 7

was taken with a G of 7 and the blue was taken with a G of 9.

The detector signal i_0 is the straight-through intensity of the beam at a particular wavelength λ' and is a reference intensity for our measurements. The synchrotron spectrum, the diffraction grating, and other filters can all cause i_0 to vary for different wavelengths. Assuming that i_0 did not fluctuate significantly with time, scans were taken periodically instead of before every $R(\lambda', \theta)$ set. To take the scan, we lowered the sample stage below the beam and moved the detector to zero. We scanned the diffraction grating through a wavelength range that encompassed the desired λ' and recorded the straight-through intensity. We obtained a smooth data curve that looks like Figure 2.8 . A number of reflectance sets use this same i_0 data, therefore we did not always precisely sample the desired wavelength. In our data analysis, we interpolated the data and then selected the value of the function at the desired wavelength.

Even with the light completely blocked, the detector produces a very small current that the computer records as a signal. This noise is called dark current DC and is caused by the thermal recombination of electron-hole pairs in the photodetector. We accounted for the dark current by averaging over time and subtracting that value from our data. To record the dark current, the detector was moved to zero and the

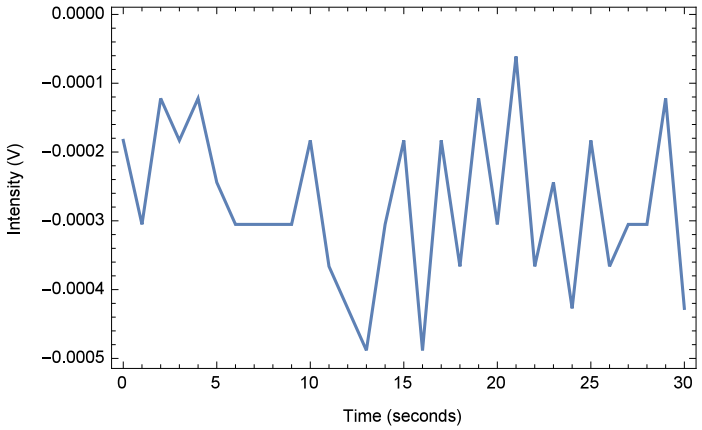

Figure 2.9: A typical dark current reading, read with a G of 7.

sample stage was rotated to 90°, completely blocking the detector from the incoming light beam. Before or after each reflectance measurement, we ran the detector for about 30 seconds at a corresponding gain G. Figure 2.9 shows a plot of a dark current measurement. When the amplifier gain is raised to account for a smaller overall reflectance signal at larger angles, this dark current is also amplified, thereby introducing greater error into our measurements.

The beam current BC is proportional to the number of electrons in the synchrotron storage ring. This was very stable over the course of the experiment and held a value of 500.200 ± 0.500 mA. The beam current measurement was used to normalize our data at every wavelength and angle. Because the variations in the beam current were so small, normalizing in this fashion could actually increase the uncertainty of the corrected data rather than decrease it.

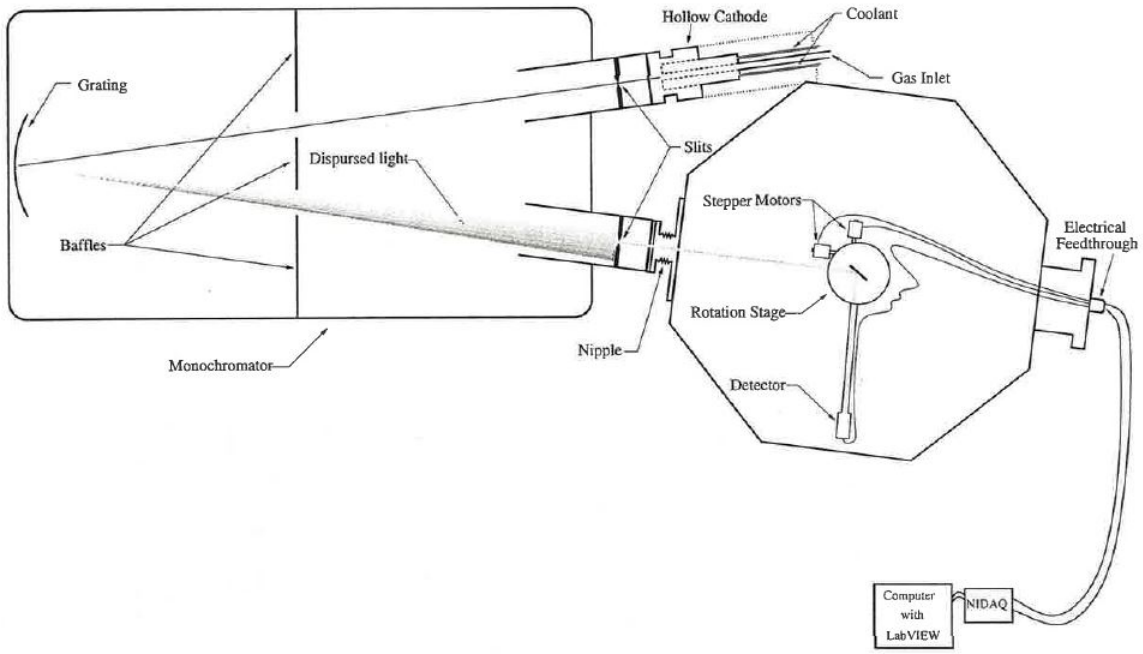

Figure 2.10: Diagram of the hollow cathode, monochromator and variable angle reflectometer system[5]

2.2 Aluminum

2.2.1 Description of BYU System

In 2001, BYU master's student Matthew Squires assembled a system to measure sample reflectance at different angles in the VUV[5]. This system contains a hollow cathode plasma discharge light source, a monochromator, and a variable angle reflectometer, as shown in Figure 2.10. In this section I will describe in greater depth the various components of this system and how we use it to measure the reflectance of aluminum.

Figure 2.11: Picture of Hollow Cathode EUV source

Hollow Cathode

We use a hollow cathode as the plasma source for our ultraviolet light. Figure 2.11 shows an image of the device in operation.

We monitor the pressure of the plasma inside the hollow cathode with a 10 torr capcitance manometer; typical base and operating pressures are around 10 and 200 millitorr respectively. Our high-voltage power supply outputs a negative voltage of about -700 V. Most of that voltage is dropped across a current-limiting 450 Ω ballast resistor placed in series with the plasma; the resistor is rated for high power. For greater stability over time, this resistor is air-cooled with a fan. As the resistor heats up, we typically wait about 30 minutes before taking data in order for the resistance to stabilize. Under normal operation we have about 1 A of current going through the hollow cathode and plasma. We typically have a voltage drop of about -400 V accross the plasma.

Light generates in the space between the cathode and the anode. The photons released by atomic/ionic collisions can pass into the monochromator through a small pinhole in the anode.

Monarch

Monarch is the name for the near-normal incidence monochromator used in our measurements, a McPhearson model 225 vacuum ultraviolet monochromator. A monochromator is a device that functions much like a prism to disperse white light into its spectral components. Instead of using refraction, however, the monochromator uses a reflective diffraction grating to disperse the light. The grating, the entrance slit, and the exit slit are the essential components of a monochromator.

Light from the pinhole is formed into a beam by the vertical entrance slit. A micrometer adjusts the width of the slit from 0 to 3 mm. Adjusting the slit width changes how much light gets into the chamber. A wider slit gives increased light intensity, but decreased spatial resolution. We are also limited by how much light the detector can handle before the detector becomes damaged.

The diffraction grating is curved with a focal length of 1 m. It has a blazed ruling of 600 lines/mm. The grating holder rests in a kinematic mount on a pivoting arm. A stepper motor moves the arm from side to side, thereby changing the angle of the grating but keeping its focal point on the exit slit.

The exit slit has the same orientation, design and mechanics as the entrance slit. The entrance and exit slits must be set to the same widths in order to optimize both intensity and spatial resolution.

Since VUV and EUV cannot propagate in a space with air or other gases, the monochromator is kept at a base pressure of 10^{-6} torr. By design, helium gas leaks through the anode pinhole when the plasma is running. Therefore, we see operating pressures in Monarch typically around 10^{-5} torr.

I aligned the pinhole, the slits and the grating with a green laser (532 nm) shining through the gas inlet tube of the hollow cathode. I mounted the laser in a kinematic mirror mount which was placed on an XY translation optic post holder. This allowed

me to precisely position the laser spot directly down the center of the gas line with control over the position and angle of the beam. The laser beam reflects specularly off the grating at the zeroth order diffraction peak and focuses on the exit slit. In aligning the pinhole and the slits with the laser beam, I was able to calibrate the position of the grating.

Octopus

Octopus is the name for the octagonal chamber containing the variable angle reflectometer. It is connected to Monarch via a bellows flange at the monochromator's exit slit. A rotary butterfly valve separates the two chambers. Light from the exit slit passes through another attenuating pinhole, reflects off the sample on the rotating stage and passes into the photon detector. The pin hole reduces the intensity of the light, but it increases the spatial resolution of the beam. This allows us to measure reflectances from a smaller region on our samples. Diffractive effects from the pinhole can be ignored since its diameter is large compared to the wavelength of EUV light.

The sample stage contains three stepper motors for x, y, and z translation. It also contains a stepper motor to rotate the entire assembly by an angle θ.

The intensity of light is measured using a MD-501 Amptektron® made by Amptek Inc. Inside the MD-501 is a channel electron multiplier (CEM) which detects the light. The inner walls of the CEM are lined with an photoelectric material that creates an electron avalanche when hit by high-energy radiation. 2.4 kV across the CEM accelerate the electrons towards the detector. For every photon, around 10^7 electrons are ejected from the CEM surface and then detected by a charge collector circuit. If you operate the CEM at pressures higher than 10^{-4} torr, the high voltage creates an internal corona discharge which can destroy the electronics and the inner surface of the CEM. The detector is mounted on an aluminum arm and is oriented to the inside

of the chamber. A stepper motor pivots the arm by an angle ϕ.

O-ring flanges on Octopus preclude the option of baking the system and going to even higher vacuum. By itself, the chamber achieves a minimum pressure of 2×10^{-6} torr. When the hollow cathode source is operating, the pressure is around 1×10^{-5} torr due to the intentional helium leak.

2.2.2 Problems to Address

Hollow Cathode Heating

We observed that the hollow cathode was not as resilient to temperature changes as we had hoped. The water coolant did a good job at keeping the main mass of the hollow cathode cool to about 30° C, but at currents higher than 1 A, the temperature of the metal segment of the gas inlet line increased to over 100° C. At about 1 kV and 1.8 A on the power supply, this metal tube began to glow red hot. The gas inlet tube is thermally and electrically insulated from the rest of the gas line by a hollow glass tube, an important safety feature. We considered building a circulating water jacket to surround the tube but this was too complicated for immediate implementation. We determined, for the present, to sacrifice light intensity for safety by operating at 1 A or less at all times.

Insulating Disk Melting

Occasionally, the water would not flow correctly either due to an operation error or an obstruction in the water line, preventing the cathode from cooling. When this occurred, the hot cathode would melt the polycarbonate insulating disk and physically deform it. This would release the vacuum to atmosphere and completely disrupt the plasma. The polycarbonate is a good material because it is cheap, easy to machine

Figure 2.12: Fractured Macor® insulating disk

and transparent to visible light, however, it is very susceptible to melting. Although the process of making a new polycarbonate disk is simple, it costs several days of machining and assembly every time it fails.

We wanted to try a different material that would likely require less frequent replacements. We chose to make the disk out of Macor®, a white machinable ceramic that is much more thermally resistant. The design of our disk includes four inset helicoil screw holes that the hollow cathode bolts into. When I tightened the hollow cathode bolts, the tension caused micro-fractures to form in the ceramic. Because ceramic is such a brittle material, these micro fractures propagated and left large cracks in the surface of the disk, exposing the plasma chamber once again to atmospheric pressure. Figure 2.12 shows the disk with the fractures clearly visible around the center bottom left screw insert. We concluded that Macor® is not a good material for the insulating disk without majorly redesigning both the disk itself and the hollow cathode.

In the future, we hope to try a different material that is strong, but both thermally and electrically insulating. An idea that we had was to make the same disk out of

aluminum and then coat the front and back surfaces with Kapton® tape, an adhesive commonly used in vacuum systems. Kapton® tape is non-volatile and is a very good insulator. We measured that a Kapton® film has a resistance in excess of 20 MΩ, more than enough for our needs. The aluminum will provide sufficient strength and is reasonably cheap and machinable.

Power Supply Instability

As I have previously discussed, the characteristics and stability of the plasma source are greatly affected by the voltage and current that we supply to it. Ideally, the voltage and current would both be perfectly constant. We use a Universal Voltronics DC power supply that gives a voltage 1–2500 V and a current 0–2 A. While attempting to connect the power supply to our data acquisition system, we observed around a 10% 120 Hz AC ripple on top of the 700 V DC. We remedied this by placing a high-voltage capacitor in the circuit and providing better grounding and shielding for many of the other wires. The deviations in the power supply are now significantly less than 1%.

Spots on the diffraction grating

While working on the monochromator, we noticed that the surface of the diffraction grating was speckled with little while dots shown in Figure 2.13 . We concluded that the spots were either water deposits from a previous flooding event in the chamber or roughing pump oil that had leaked back into the system and deposited onto the grating. Contaminants on a grating like this are usually irremovable and can render the optic useless. We saw that the spots did indeed scatter light and give us a higher background level for our spectroscopic peaks.

Figure 2.13: Spots on the diffraction grating

2.2.3 Procedure

Our first step in characterizing our EUV light source was to measure its spectrum. To do this, we reversed the orientation of the detector so that it was facing to the outside of the chamber and placed it directly in front of the Monarch exit slit. The diffraction grating was set to zeroth order so that all light incident upon the grating was reflected specularly. We sampled the light intensity on the detector along a small range of angles on each side of the slit to obtain a light intensity curve like the one shown in Figure 2.14 . From there, we located the center maximum of the peak and zeroed the detector on that angle. The fringe peaks shown in this plot were common and likely due to variations in brightness across the plasma beam.

We then scanned the angle of the diffraction grating and recorded the number of photon counts from the detector at each wavelength. Especially at lower wavelengths from 0–800 , we saw a back and forth jumping pattern in the data that appeared to be a systematic data acquisition error. This problem was not fully resolved due to the subsequent failure of the hollow cathode system. This pattern can be clearly observed in Figure 2.15 which features data taken around 58.4 , the $2p \rightarrow 1s$ electron

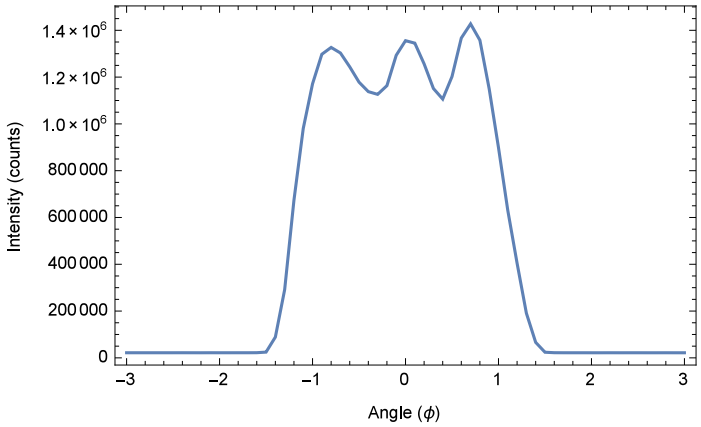

Figure 2.14: A typical detector zero positioning scan

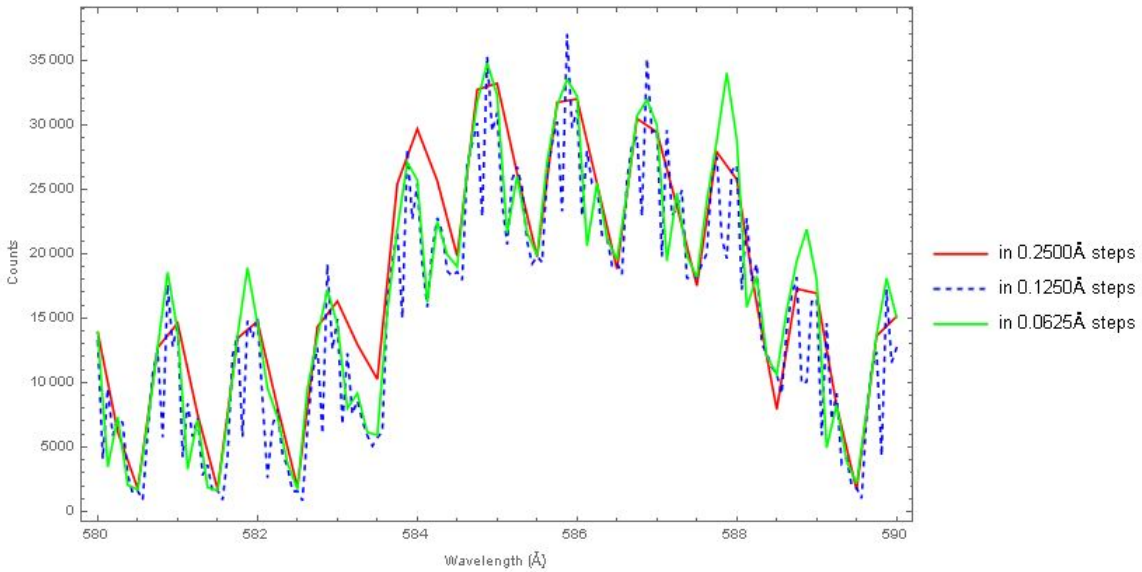

Figure 2.15: Alternating pattern around 584 Å

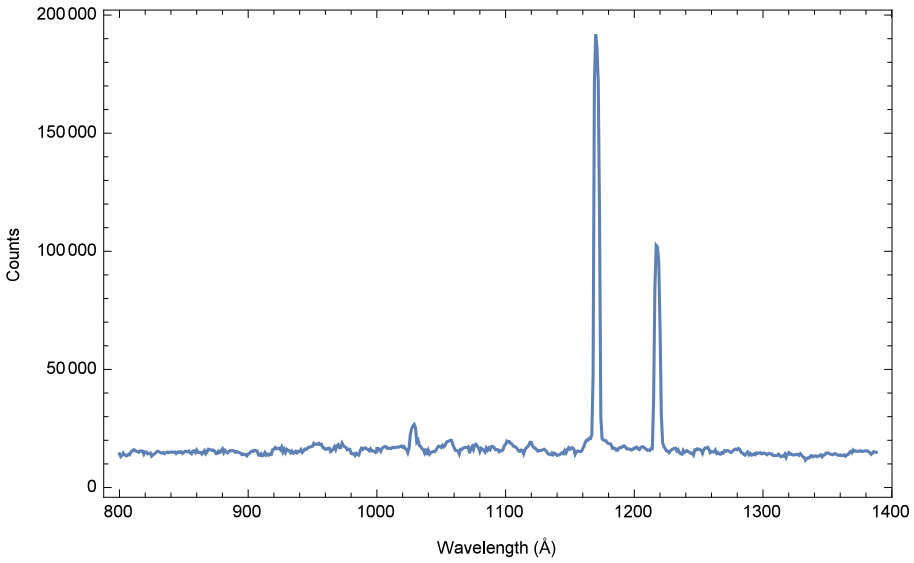

Figure 2.16: A spectrum of our source from 800 Å to 1388 Å

transition of neutral helium. The overlaid plots correspond to different step sizes, highlighting some of the hidden features of the alternating pattern.

This pattern became negligible at longer wavelengths. Figure 2.16 shows our spectral data from 800–1388 . We saw a small peak at 1029 as well as two large peaks at 1700 and 1210 .. Since we are flowing helium into the hollow cathode, it was surprising that 584 line shown previously was so dim. Apparently, the energy had gone into other transitions. We identified the last line as the hydrogen Lyman α[24]. The other two peaks could be any other sort of contaminant such as carbon, nitrogen, or oxygen. We could not distinguish the atomic species based on comparisons between our data and the NIST Atomic Spectra Database.

Chapter 3

Analysis

3.1 Yttrium Oxide

3.1.1 Data Normalization and Combination

The first part of the analysis process involved preparing the data and forming it into something meaningful. This consisted of normalizing the data to unity and then combining the different segments of the $R(\theta)$ scans, repeated for each wavelength. The **rdata.m** method that accomplished this is included in Appendix A.2. We averaged the dark current ($\overline{DC}$) at a particular gain and subtracted that value from the corresponding $R(\theta)$ or i_0 data set. We then divided the difference by the corresponding beam current (BC) and gain (G). This is shown in the following equations. The accents ($'$) identify the measured values corresponding specifically to the i_0 scans rather than the reflectance scans. This process is summaried by the following formulas

$$I_r = \frac{R(\theta) - \overline{DC}}{BC \cdot G} \tag{3.1}$$

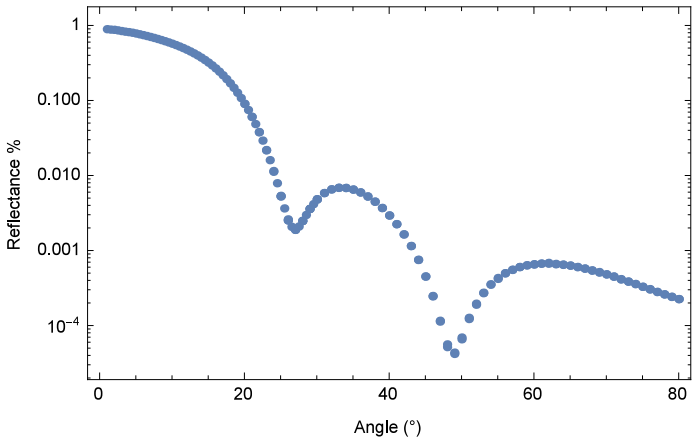

Figure 3.1: Fully normalized and combined data for λ12.5 nm

$$I_0 = \frac{i_0 - \overline{DC}'}{BC' \cdot G'}. \tag{3.2}$$

We then combined the various angular segments of the scans into data sets that spanned the angular range 2°–80°. Fully normalized reflectance data ($\mathcal{R}(\theta)$) is achieved by dividing

$$\mathcal{R}(\theta) = \frac{I_r}{I_0}. \tag{3.3}$$

Figure 3.1 shows a completely normalized and combined data set.

Especially at shorter wavelengths, there were cases where R_N became extremely noisy at larger angles, like in Figure 3.2 . This makes fitting a formula to the data practically impossible. In these situations, I chose to fit to the data that followed a smooth curve, terminating at some angle less than 80°. In the case of the data shown in Figure 3.2, I only kept the data up to 35° where the curve had less noise. Usually the data at wavelengths shorter than 8.5 nm were impossible to work with; at this scale, the wavelength is comparable to surface roughness and other features. This has a tendency to extinguish the interference fringes, as you can observe in Figure 3.23.2.

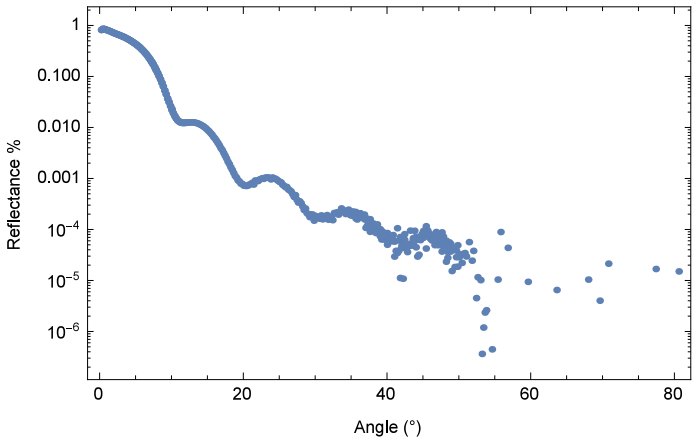

Figure 3.2: A plot of bad data, taken with λ6.5 nm light

3.1.2 Fitting Routine

To fit to my data, I used the *Wolfram Mathematica*® NonLinearModelFit routine. It's a least-squares method of fitting a model function to a data set. This routine accepts:

1. The data (θ,$R(\theta)$) in a coordinate paired list.
2. A mathematical model that includes independent variables and fitting parameters. We used the Parratt recursion formula with a Debye-Waller roughness factor.
3. A paired list of each fitting parameter and an initial guess.
4. The independent variable θ.
5. A weighting function.

This routine returns:

1. The function of the fit
2. The value of each fitted parameter

3. The standard error in each parameter

3.1.3 Method of Fitting

Based on the film growth procedure, we made a simple model of its composition: a thick silicon substrate layer, a thin (<5 nm) silicon dioxide layer and a layer of yttrium oxide with roughness on top. We fit the Parratt formula for this stack to the reflectance data using an iterative, user input method. Since the NonLinearModelFit routine is sensitive to initial guess of the fit parameters, I had to continually refine my guesses until the fit curve matched visually, as good as possible, with the data. For each data set, I started the fitting process by guessing a Y_2O_3 layer thickness of 17 nm, a value that Allred had obtained through ellipsometry. There were certain values that I initially did not let the routine fit, such as the RMS roughness, and the thickness of the SiO_2 layer; they were given the typically expected values of 1.6 nm and 1.5 nm, respectively. In all of the fits, I used a value of 1 for the index of refraction of the vacuum.

I used the Reflective X-ray Optics IMD database of optical constants in my fitting[25]. The values for the optical constants were calculated using the CXRO atomic scattering factors. In all of my fitting, I used the IMD value of the index of refraction of the silicon substrate. For the Y_2O_3 layer, I used the IMD value of the index as a starting guess.

The NonLinearModelFit routine accepts a weighting function. This provides to the least-squares method a preference of fitting to some data points over others. Figure 3.3 shows some typical reflectance data that varies by up to four orders of magnitude. By itself, the fitting routine will fit really well to the low-angle data, but horribly to the higher angle data. The weighting function instructs the routine to give a preference to a data point inversely proportional to the square of the data

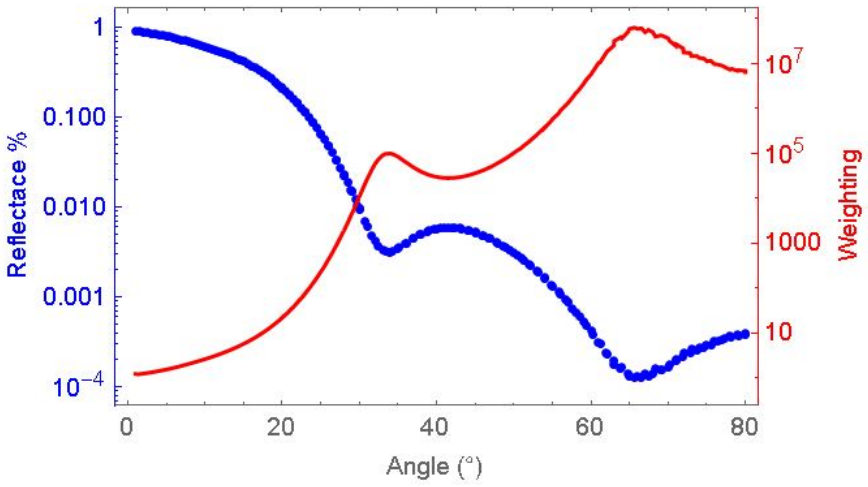

Figure 3.3: Data for λ15 nm and its weighting function

point's value. In summary,

$$W(\theta) = \frac{1}{R(\theta)^2}. \tag{3.4}$$

The first fit using the initial guesses and assumptions was usually not very accurate, but it did give me a ballpark range for the layer thicknesses. If the interference fringes were shifted from, closer together than or further apart than the data, it typically indicated that the layer thicknesses weren't correct and I adjusted my guesses. Sometimes the fringes dipped significantly below the data and I could account for this in a variety of ways; higher initial guesses in the SiO_2 layer thickness and in the RMS roughness usually helped to smooth out the reflectance. I found that letting the routine fit the real and imaginary parts of the Y_2O_3 index of refraction almost universally improved the fit. Sometimes, the routine provided fit parameters that were non-physical, such as negative thicknesses or roughness. These were generally discounted and other initial guesses were supplied. These fits were repeated for every wavelength that we sampled from 4.5–31 nm. We measured and fit multiple data sets

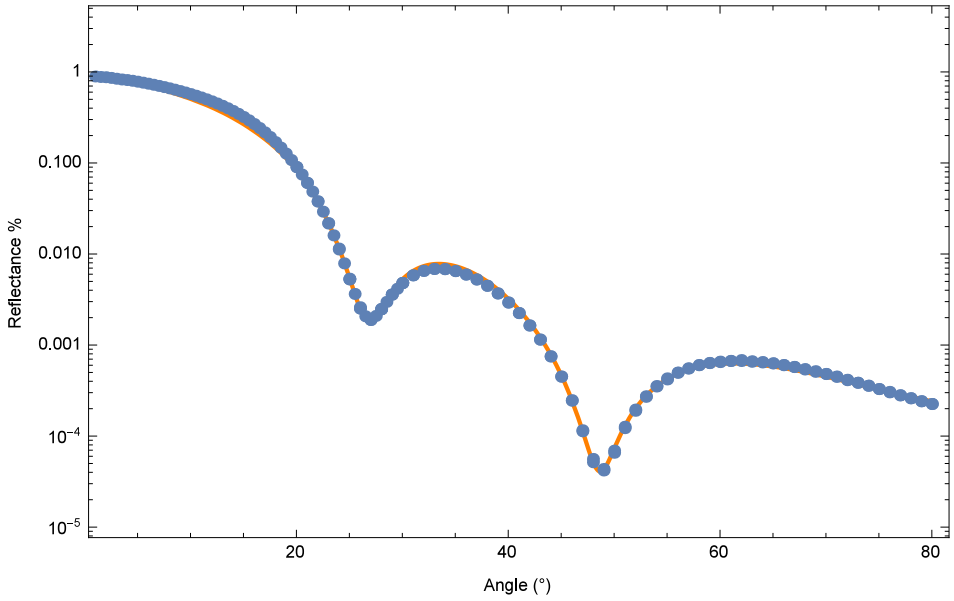

Figure 3.4: A typical fit that was considered very good at λ12.5 nm

of reflectance for the wavelengths 5.5, 9.5, 11.5, 12.5, 13.0, 15.0, 18.0 and 30.0 nm.

The least-squares method attempts to minimize the error in a large fitting parameter space by systematically adjusting each parameter. Depending on the initial guesses of the fitting parameters, the method can settle at an inaccurate local minimum of the error rather than global minimum. Changing the guesses will allow the error to settle at a different minimum. When adjusting the initial guesses, it's important to vary the guess for only one parameter at a time and to make incremental rather than large-scale changes.

Figure 3.4 shows one fit that was very good, taken at 15 nm. One of the worst fits that we encountered is shown in Figure 3.5 , taken at 10.5 nm. You can see that the fringe peaks are in the right place, indicating a good fit to the sample thickness. However, roughness and other irregular features have broadened and raised the peaks.

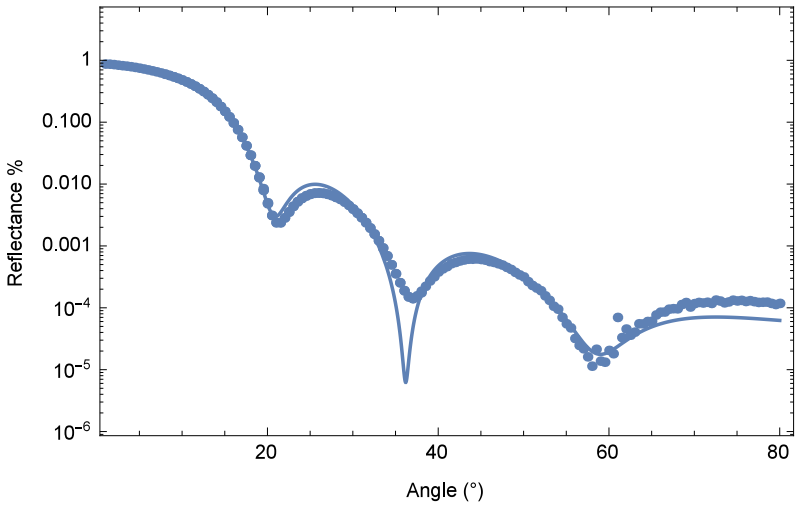

Figure 3.5: One of the worst fits at λ10.5 nm

Chapter 4

Results and Conclusions

4.1 Fitting Results

I will provide in this section the fitting results for the optical constants δ and β, as well as the fitted values for the Y_2O_3 layer thickness, the SiO_2 layer thickness and the RMS roughness. These values will be given for wavelengths from 8.5–31 nm. The standard error of the fit parameters for each wavelength were included as error bars on the plot points. Data from wavelengths that were sampled multiple times are superimposed on the plots.

4.1.1 Optical Constants

Figure 4.1 and Figure 4.2 summarize the results of the optical constants from the least-squares fitting of the Parratt formula. Both constants appear to follow a smooth curve. δ increases in an almost linear fashion from 0.02 to 0.24 over the wavelength range. The imaginary part β increases exponentially by about the same amount over this range. Intuitively this makes sense. X-rays are extremely penetrating while ultraviolet light is not, so we would expect β to be higher at longer wavelengths than

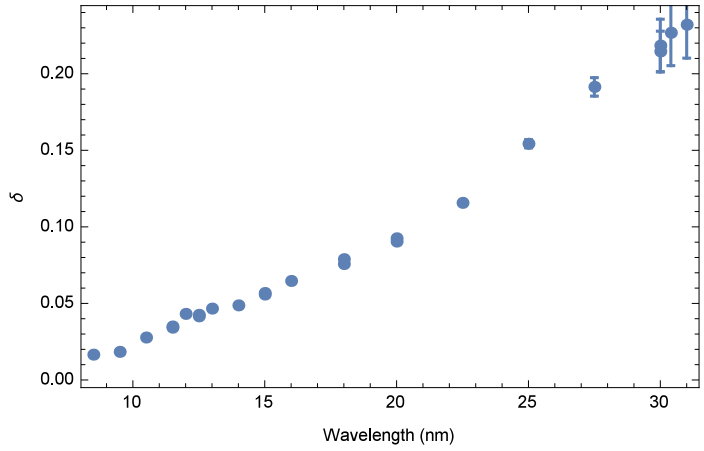

Figure 4.1: Fitted real part (δ) of the index of refraction for λ8.5–31 nm

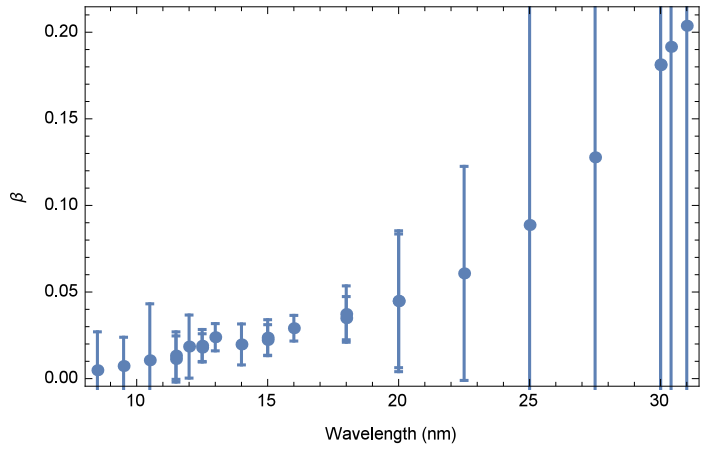

Figure 4.2: Fitted imaginary part (β) of the index of refraction for λ8.5–31 nm

shorter ones. The fitting produced an overall greater uncertainty for each of the β data points.

4.1.2 Layer Thicknesses

Since we measured reflectances from a single physical site on our sample, we should expect that the thicknesses of the Y_2O_3 and SiO_2 layers to be the same at all wavelengths. We achieved the best fits, however, when we allowed the least-squares routine to vary the layer thicknesses. Figure 4.3 and Figure 4.4 show as a function of wave-

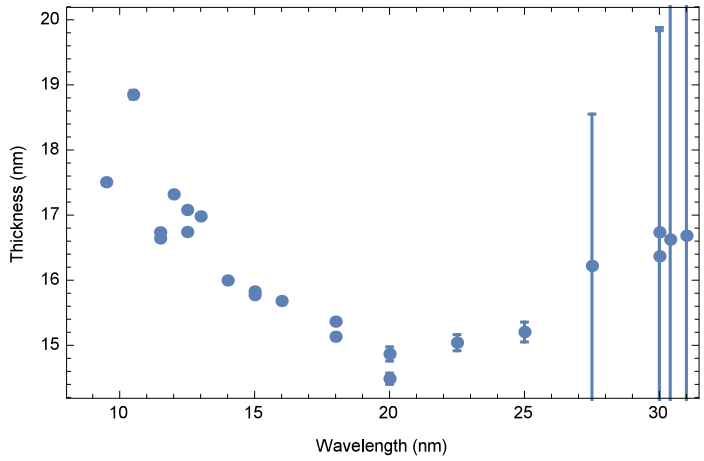

Figure 4.3: Fitted thicknesses of Y_2O_3 layer for λ8.5–31 nm

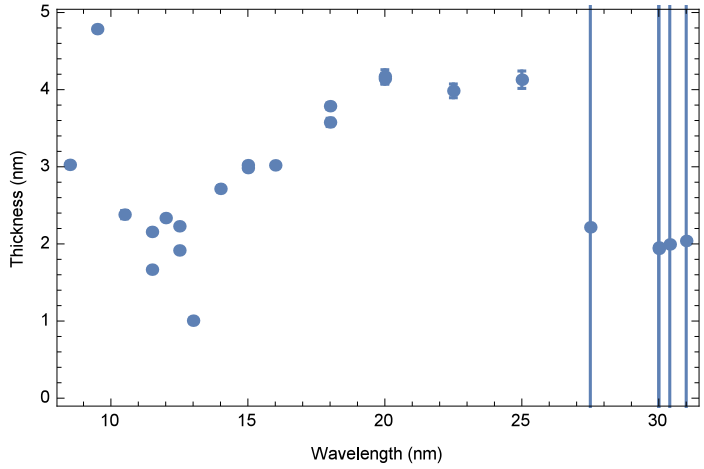

Figure 4.4: Fitted thicknesses of SiO_2 layer for λ8.5–31 nm

length the fitted thickness of the two layers respectively. The standard error on these parameters at each point was relatively low below 27 nm and became very large above that. Both layers when fitted displayed parabolic behavior as a function of wavelength with the vertex at 20 nm. The average thickness of the Y_2O_3 layer was 16.53 nm with a standard deviation of 1.676 nm. This is close to the 17 nm value that Allred estimated using ellipsometry. The average thickness of the SiO_2 layer was 2.80 nm with a standard deviation of 0.978 nm. Using ellipsometry, Allred reported a SiO_2 layer thickness of about 3 nm. This agrees nicely with our fitted results.

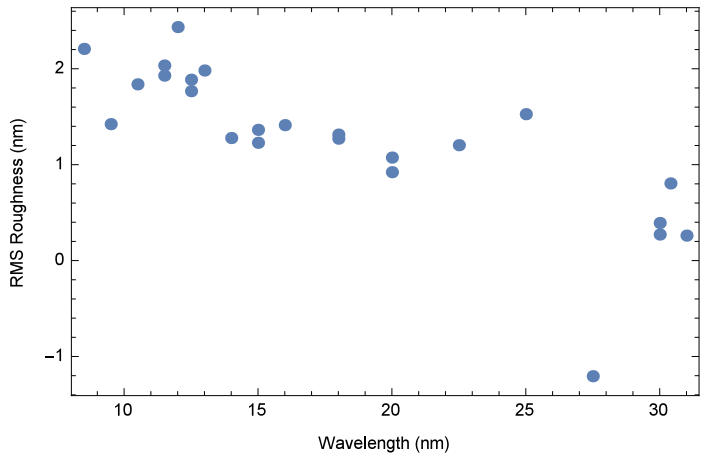

Figure 4.5: Fitted RMS roughness on the surface for λ8.5–31 nm

4.1.3 Roughness

The RMS roughness should also have been a single value for each wavelength that we sampled, but we similarly achieved better overall fits when we let the least-squares fitting routine vary the roughness. The data for RMS roughness is summarized in Figure 4.5 . The trend of the roughness appears to be decreasing for lengthening wavelengths. This makes sense because at longer wavelengths the surface will appear smoother and reflect more like a perfectly flat shiny mirror instead of a dull matte surface. The standard error for each data point is relatively low. I initially computed an average RMS roughness of 1.28 nm with a standard deviation of 0.784 nm. Looking at my data, I realized that there was a non-physical outlier - a *negative* roughness - as you can see in Figure 4.5 at 27.5 nm. Occasionally in the fitting, negative values emerged for fit parameters and this usually required that I adjust my initial guesses until the negative values went away. For the case of 27.5 nm, I allowed the roughness to go negative in order to make the other fit parameters even reasonable. You can see in this and in the other plots that 27.5 nm had one of the largest errors of all the wavelengths that I fit. When I removed the outlier, the average RMS roughness was 1.38 nm with a standard deviation of 0.592 nm.

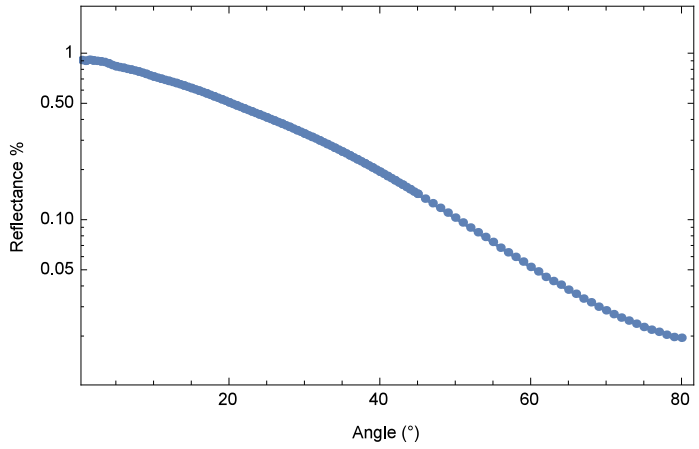

Figure 4.6: Reflectance at $\lambda 30\,nm$

It's worthy to note that the fitted RMS roughness is larger than the value we obtained from the AFM by about a factor of 10.

4.2 Uncertainties

The uncertainty in the fitting parameters at each wavelength were the standard error calculated from the least-squares fitting routine.

We saw that this uncertainty was much higher at longer wavelengths. In this region, first of all, the reflectance curves that we fit to did not contain many distinguishing features. For example, there were no interference fringe dips and the curve dropped steadily downwards, as in Figure 4.6 . We don't see as many fringes at these longer wavelengths because the wavelength of light is too large to see destructive interference effects. Where there are not as many features on the curve, the fitting routine has a great deal of freedom in the fitting parameters; big deviations in the parameters can produce almost identical fit curves. For this reason, there is much more uncertainty in the fits at longer wavelengths than at shorter ones.

However, the uncertainties represented on these plots is deceiving. Optical con-

stants are physical quantities that change smoothly and follow a specific trend over a given wavelength range. Even though the error bars for each point extend far outside of the trend curve, the mean values of the fitted data behave exactly as we would expect. This highlights the difference between statistical errors vs. systematic errors.

Statistical error comes from the random nature of measurements. If I flip 10 coins, then I could possibly get a head/tail ratio, for example, of 7:3. This doesn't mean that there is a 70% probability of getting a head (for a fair coin). It rather means that there is some statistical error in the measurements that I am making. If I flip 100 coins or even 10,000 coins, you would naturally expect that the ratio would approach 50:50. By making more repeated measurements, you can reduce the statistical error.

Systematic error comes from trying to fit the wrong formula to a set of data. In our reflectance measurements, we constructed a model and a formula that contained various assumptions about the composition (what is it *really* made of), the structure (solid, voids, pillars) and the interfaces (flat and rough). However, it's very likely that we simply do not have all of the information about the material packaged into our model. Therefore, when we try to fit our model to the real data, they don't *exactly* match because they represent two different materials. Therefore, this gives a much larger error in the fit than is really meaningful.

We can separate the systematic error from the statistical error if we don't require any particular function to fit the data. We can fit a cubic spline curve to the data, a piecewise polynomial fucntion with continuous values, first and second derivatives at each of the "knots". The cubic spline tries to minimize two factors scaled by a factor λ: 1) the average error between the data points and the curve Δ and 2) the sum of the squares of the second derivatives. Therefore, we can obtain a smooth curve that passes through the middle of all the data. With a λ of 0, the spline goes through every point and is quite wiggly. For increased λ, the spline gets smoother and passes

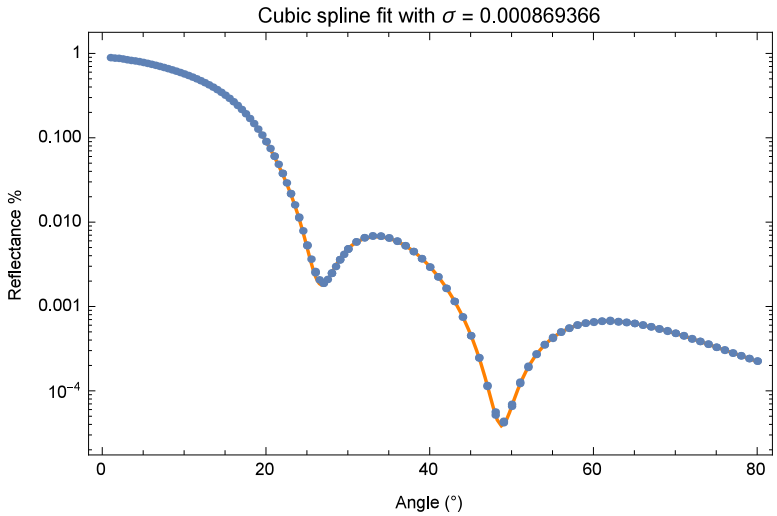

Figure 4.7: Cubic spline fitting and RMS error for λ12.5 nm

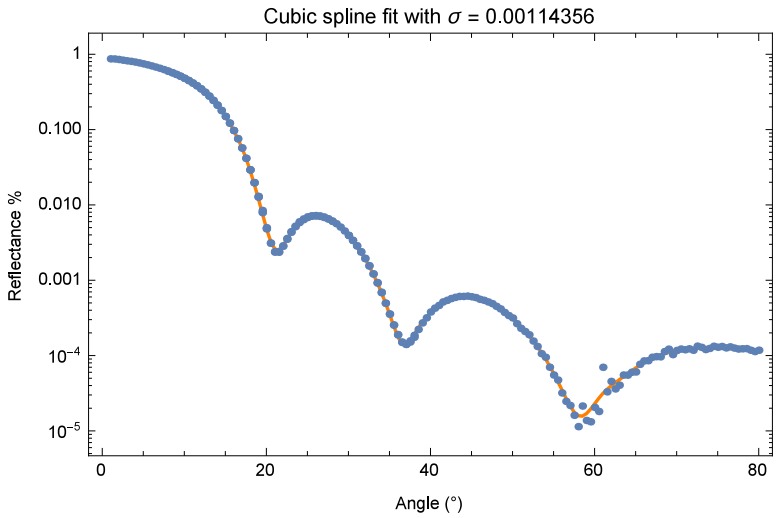

Figure 4.8: Cubic spline fitting and RMS error for λ10.5 nm

more through the average of the points. With a very high λ, the curve becomes too smoothed and important features of the data are washed out.

We can smooth the data and then find σ, the RMS deviations of the data from the spline curve fit. I will show this process for two different reflectance curves, one for which the Parratt formula fit was very good, shown in Figure 3.4, and one for which the fit was not good, shown in Figure 3.5. Figures and show the results

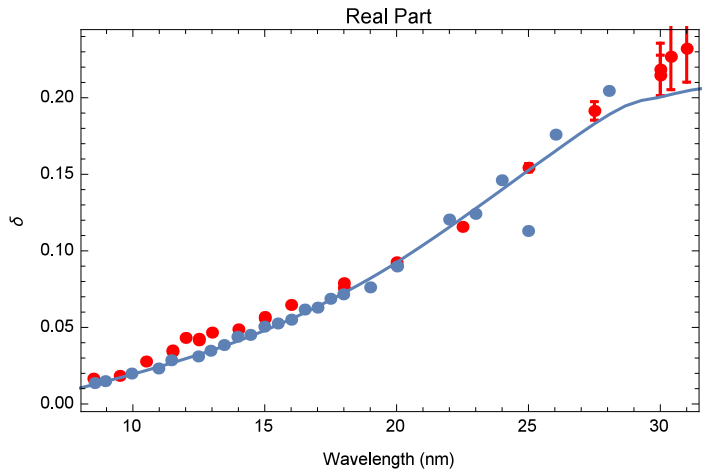

Figure 4.9: δ for our data (red dots), Muhlestein's data (blue dots), and the CXRO data (blue line)

of the spline fittings respectively together with their σ. The RMS deviations from the spline σ were 0.0867% and 0.114% respectively. These are the statistical errors in our measurements and are significantly smaller than the error provided by the least-squares routine. Therefore, we are justified in using smaller error bars in our plots.

4.3 Comparisons

Figures 4.9 and 4.10 show our data overlaid on plots of Muhlestein's 2009 data and the CXRO calculations. Muhlestein only measured the optical constants up to 28 nm and we were able to extend the range up to 31 nm. For δ, our data matched very well with the previous data. However, at the longest wavelengths, our values for δ were about 10% larger than the CXRO calculations, even with the added uncertainty in that region. β from our data was also about 5% larger than in the former data, although these are still within the uncertainties of our measurements.

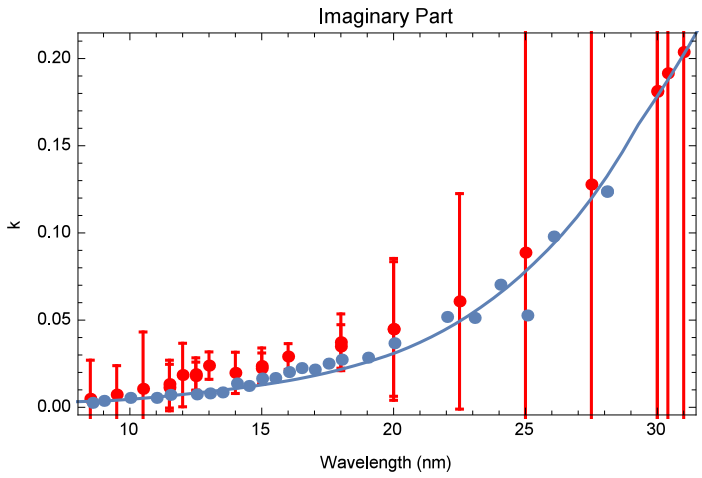

Figure 4.10: β for our data (red dots), Muhlestein's data (blue dots), and the CXRO data (blue line)

4.4 Conclusions

4.4.1 Yttrium Oxide

We were able to measure the optical constants of Y_2O_3 in the EUV range of the electromagnetic spectrum. The results were similar to the previous measurements, but contained some slight differences, especially in the imaginary part β. In order to completely reduce the uncertainties in our measurements of the optical constants of Y_2O_3, we would need to preform additional reflectance measurements with thicker films. If the film thickness were closer to 30 nm, then we could distinguish interference fringes patterns in that region.

4.4.2 Aluminum

Future work will need to be done once we have a reliable, contaminant-free system.This includes further testing of the diffraction grating in order to obtain consistent spectra from our plasma source. Different noble gases will need to be tested in order to find transition lines in the desired wavelength region. Octopus will receive

an extension that will allow us to evaporate aluminum films while under vacuum.

Appendix A

Parratt Formula Code

A.1 refl.m

The function `parrattRough` returns the reflectance of a thin film stack on a substrate as a function of θ. It accepts:

1. A list of index of refraction/film thickness pairs. Both the substrate and the vacuum are given a thickness of 0 in this formula. We let the NonLinearModelFit routine fit the thicknesses and indices of refraction of the SiO_2 and the Y_2O_3 layers.

2. The independent variable θ.

3. The wavelength of the light λ. Since we knew this value with good precision, this value was not fit with the NonLinearModelFit routine.

4. The percentage of s-polarization of the light. This fraction was given to be 0.9 for the wavelengths that we sampled[13].

5. The Root Mean Squared (RMS) roughness of the surface. Surface roughness defects on the scale of the wavelength of light can drastically affect the reflectance.

Although not completely descriptive, this single RMS parameter can be useful for characterizing these deviations. A rough surface is covered with peaks and valleys. RMS is the square root of the mean of the squares of the deviations from the average surface height. To properly calculate the RMS, you find the average height of the surface; this will lay above some of the valleys and below some of the peaks. You then find the distance from each sampled point on the surface to the average height and square all of those values. You take the average of all of those squared distances and then take the square root. It's a quantity for the average surface deviations from a mean height. In summary,

$$RMS = \sqrt{\frac{1}{NM}\sum_{i=1}^{N}\sum_{j=1}^{M}(h(x_i, y_j) - \mu)^2} \tag{A.1}$$

where h is the height of the surface at any point (x_i, y_j) and μ is the average height of the surface. We let the NonLinearModelFit routine fit the RMS roughness of the top Y_2O_3 layer.

```
BeginPackage["refl`"]

refl::usage = "refl is a collection of routines related to
    finding optical and physical properties of thin film
   optics.  It includes the routines parrattR,
   parrattRough, matR, imdFile, imdMenu, imdIndex,
   imdIndexAt, imdIndexFunction."

parrattRough::usage = "parrattRough[nd, theta, lambda,
   fractionS, sigma] returns the reflectance of a stack of
    thin films on a substrate (which could be a vacuum).
```

```
   The list nd is a list of index of refraction/thickness
   pairs with the substrate as the first element and the
   vacuum usually as the last element.  The thickness of
   the substrate and vacuum layers should be set to zero.
    The argument theta is the angle of incidence and
   reflection measured from grazing on the vacuum side in
   degrees.  The lambda argument is the wavelength
   wavelength using the same units as the layer thickness.
     The fractionS argument is the intensity of the s-
   polarized component of the incident light.  The
   calculation is corrected for roughness of the top
   interface between the vacuum and top layer having a
   surface rms roughness of sigma using the Debye-Waller
   correction. This calculation is faster than using the
   matrix formula in matR if only reflection is desired."

imdFile::usage = "imdFile[] returns a list of strings of
   filenames with index of refraction in them."

imdMenu::usage = "imdMenu[selection] draws a menu button
   which returns the selected file name with index of
   refraction data as the value of the argument selection
   on return."

imdIndex::usage = "imdIndex[file] returns a list of the
   complex index of refraction stored in file."
```

```
imdIndexAt::usage = "imdIndexAt[file, wavelength] returns
   the complex index of refraction from file interpolated
   to the given wavelength measured in nanometers."

imdIndexFunction::usage = "imdIndexFunction[file] returns
   the interpolation function of the index of refraction
   in file."

Begin["`Private`"]

parrattRough[nd_, theta_, lambda_, percentS_, sigma_]:=
   Module[{rs, rp, Si, fs, fp, k, Ci, f, Ci12, q, dbf},
         k:=2*Pi/lambda;
         Si[ni_]:=Sqrt[ni^2-Cos[theta*Pi/180]^2];
         Ci[ni_, di_]:=Exp[2*I*k*Si[ni]*di];
         fs[n1_, n2_]:=(Si[n1]-Si[n2])/(Si[n1]+Si[n2]);
         fp[n1_, n2_]:=(n2^2*Si[n1]-n1^2*Si[n2])/(n2^2*Si[
            n1]+n1^2*Si[n2]);
         rs=0;
         rp=0;
         For[i=2, i<=Length[nd],i++,
                 f=fs[nd[[i,1]],nd[[i-1,1]]];
                 If[i==Length[nd],
                         q=4 Pi Re[nd[[i-1,1]]]/lambda Sin[
                            theta*Pi/180];
```

```
                        f=f*Exp[-q^2 sigma^2/2];
                ];
                Ci12=Ci[nd[[i,1]],nd[[i,2]]];
                rs=Ci12*(f+rs)/(1+f*rs);
                f=fp[nd[[i,1]], nd[[i-1,1]]];
                If[i==Length[nd],
                        f=f*Exp[-q^2 sigma^2/2];
                ];
                rp=Ci12*(f+rp)/(1+f*rp);
        ];
        percentS*Abs[rs]^2+(1-percentS)*Abs[rp]^2
]

imdFile[]:=Module[{nkLines,nkFiles},
        nkFiles=Import["http://volta.byu.edu/nk","HTML"];
        nkLines=StringSplit[nkFiles,"\n"];
        First[StringSplit[#]]&/@ nkLines[[6;;-3]]
]

(* Read the index of refraction data from a file *)
dataList[file_String]:=Module[{nkDir="http://volta.byu.edu
   /nk",nkData},
        nkData=Import[StringJoin[{nkDir,"/",file}],"Table
           "];
        (* just keep the header information *)
        nkData=Select[nkData,MatchQ[First[#],_Real]&];
```

```
        (* convert to nm and complex numbers *)
        Map[{#[[1]]/10,#[[2]]+I #[[3]]}&,nkData]
]

imdMenu[selection_]:=Module[{names},
        names=imdFile[];
        PopupMenu[Dynamic[selection],names]
]

imdIndex[file_String]:=Module[{data},
        data=dataList[file];
        Fold[If[MemberQ[Map[First,#1], First[#2]],#1,
           Append[#1,#2]]&,{},data]
]

imdIndexFunction[file_String]:=Module[{goodList},
        goodList=imdIndex[file];
        Interpolation[goodList]
]

imdIndexAt[file_String, wavelength_Real]:=Module[{ifunc},
        ifunc=imdIndexFunction[file];
        ifunc[wavelength]
]

End[]
```

```
EndPackage[ ]
```

Appendix B

Atomic Scattering Factors

The equation of motion for a single electron s is given by

$$m\frac{d^2x_s}{dt^2} + m\gamma\frac{dx_s}{dt} + m\omega_s^2 x_s = -eE_0 e^{-i(kx-\omega t)} \tag{B.1}$$

where $x_s(t)$ is the motion of the electron, the damping factor γ is due to energy lost in collisions and ω_s is related to the attractive Coulomb force from the nucleus. We solve this equation by assuming that the electron oscillates at the same frequency as the incoming wave, or that

$$x(t) = x_s e^{-i\omega t}. \tag{B.2}$$

Eventually, it becomes clear that the resultant electric field from all the electrons is proportional to the unitless scattering factor

$$f^0(\omega) = \sum_{s=1}^{Z} \frac{\omega^2}{\omega^2 - \omega_s^2 + i\gamma\omega}. \tag{B.3}$$

At low enough energies of ω, not all of the electrons in the atom participate in scattering, therefore we can express

$$f^0(\omega) = \sum_{s=1}^{N(\omega)} \frac{g_s \omega^2}{\omega^2 - \omega_s^2 + i\gamma\omega} \tag{B.4}$$

as a sum from 1 to the number of electrons $N(\omega)$ participating in the scattering, which depends on the energy of the light. The integer $g_s$is called the *oscillator strength* and it is equal to the number of electrons corresponding to a resonance frequency ω_s[1]. Electrons are quantum mechanical particles and these quantum effects are taken into account with g_s.

We can represent f^0 in terms of its complex components as

$$f^0(\omega) = f_1^0(\omega) - i f_2^0(\omega). \tag{B.5}$$

In practice, the values for f_1^0 and f_2^0 are determined semi-empirically from the photoabsorption measurements of atoms in their elemental form[3].

The index of refraction is related to the atomic scattering factors[18].

$$\mathcal{N}(\omega) = 1 - \delta(\omega) + i\beta(\omega) = 1 - \frac{N_a r_0 \lambda^2}{2\pi}(f_1^0 - i f_2^0) \tag{B.6}$$

Here, N_a is the atomic density of the material, r_0 is the classical electron radius (2.81794×10^{-15}m) and λ is the wavelength of light.

Appendix C

Drude-Lorentz Model

In this section, I will demonstrate how the drastic reflectance change of metals at the plasma frequency occurs using the *Drude-Lorentz model* and drawing largely from [22]; additional information can readily be obtained from most books on material optics such as [26]. We first obtain the relative permittivity of the metal ϵ_R and use that to find the complex index of refraction,

$$\mathcal{N} = \sqrt{\epsilon_R}. \tag{C.1}$$

To begin, the equation of motion for free electrons in an oscillating electric field moving in an arbitrary x-direction is

$$m\frac{d^2x}{dt^2} + m\gamma\frac{dx}{dt} = -eE_0e^{-i(kx-\omega t)}. \tag{C.2}$$

Notice the lack of the restoring term. We can use the same trial solution B.2 for the electron's displacement and obtain the form

$$x = \frac{eE_0e^{-i(kx-\omega t)}}{m_0(\omega^2 + i\gamma\omega)}. \tag{C.3}$$

This value is complex. The electric displacement is defined as

$$D = \epsilon_0 E + P \tag{C.4}$$

where E is the applied field,

$$E = E_0 e^{-i(kx-\omega t)}, \tag{C.5}$$

and P is the polarization. This is like an induced electric field that comes from the sloshing around of charges inside the material and is given by

$$P = -Nex. \tag{C.6}$$

where N is the number of electrons per unit volume and x is the electron displacement C.3.

Combining equations C.5, C.6 and C.3 into C.4 we obtain

$$D = \epsilon_0 E_0 e^{-i(kx-\omega t)} - \frac{Ne^2 E_0 e^{-i(kx-\omega t)}}{m(\omega^2 + i\gamma\omega)}. \tag{C.7}$$

Also, since $D = \epsilon_R \epsilon_0 E$ we can define the relative permittivity as

$$\epsilon_R(\omega) = 1 - \frac{\omega_p^2}{\omega^2 + i\gamma\omega}, \tag{C.8}$$

where

$$\omega_p^2 = \frac{Ne^2}{\epsilon_0 m} \tag{C.9}$$

and is called the plasma frequency. We will see why this term becomes very important.

In the case of a metal, valence electrons are weakly bound and $\gamma \ll \omega$. In this

limit,

$$\epsilon_R(\omega) \cong 1 - \frac{\omega_p^2}{\omega^2} \tag{C.10}$$

and

$$\mathcal{N} = \sqrt{\epsilon_R} = \sqrt{1 - \frac{\omega_p^2}{\omega^2}}. \tag{C.11}$$

We can use a modified form of equation 1.12 to find the reflectance of incident light off a metal surface in a vacuum (where $\mathcal{N}_1 = 1$) :

$$\mathcal{R} = \left| \frac{\mathcal{N} - 1}{\mathcal{N} + 1} \right|^2. \tag{C.12}$$

For $\omega < \omega_p$, the value of $\mathcal{N}$ is imaginary, which makes the reflectance equal 100%. This model helps explain why metals are such good reflectors. For $\omega > \omega_p$, the value of $\mathcal{N}$ is a positive real number. This makes the reflectance drop rapidly to zero as the frequency increases. ω_p then represents the transition point between good and poor reflection. Above the plasma frequency, the electrons in the metal can no longer keep up with oscillations of the electric field and the material becomes transparent.

Bibliography

[1] D. Attwood, *Soft X-Ray and Extreme Ultraviolet Radiation*. Cambridge University Press, 1999.

[2] J. L. Burch, "Imager for Magnetopause-to-Aurora Global Exploration." http://pluto.space.swri.edu/IMAGE/index.html, August 2015. (Accessed August 2015).

[3] B. Henke, E. Gullikson, and J. Davis, "X-ray interactions: photoabsorption, scattering, transmission, and reflection at E=50-30000 eV, Z=1-92," *Atomic Data and Nuclear Data Tables*, vol. 54, pp. 181–342, July 1993.

[4] J. H. Underwood, E. M. Gullikson, M. Koike, P. J. Batson, P. E. Denham, K. D. Franck, R. E. Tackaberry, and W. F. Steele, "Calibration and standards beamline 6.3.2 at the Advanced Light Source," *Review of Scientific Instruments*, vol. 67, no. 9, pp. 3372–3372, 1996.

[5] M. B. Squires, "The measurement (58.4-164.0 nm) and analysis (40.0-600.0 nm) of the atomic scattering factors of diamond and graphite," Master's thesis, Brigham Young University, 2001.

[6] Encyclopædia Britanica, "Ultraviolet Radiation." http://www.britannica.com/science/ultraviolet-radiation#ref202411, August 2015. (Accessed August 2015).

[7] K. Erikson, "Megnetospheres." http://science.nasa.gov/heliophysics/focus-areas/magnetosphere-ionosphere/, August 2015. (Accessed August 2015).

[8] J. Burch, "IMAGE Mission Overview," *Space Science Reviews*, vol. 91, no. 1-2, pp. 1–14, 2000.

[9] T. Krücken, K. Bergmann, L. Juschkin, and R. Lebert, "Fundamentals and limits for the EUV emission of pinch plasma sources for EUV lithography," *Journal of Physics D: Applied Physics*, vol. 37, no. 23, p. 3213, 2004.

[10] D. Tripathi, "EUV and coronagraphic observations of coronal mass ejections," *Journal of Astrophysics and Astronomy*, vol. 27, no. 2-3, pp. 193–200, 2006.

[11] J. Tumlinson, A. Aloisi, G. Kriss, K. France, S. McCandliss, K. Sembach, A. Fox, T. Tripp, E. Jenkins, M. Beasley, C. Danforth, M. Shull, J. Stocke, N. Lehner, C. Howk, C. Froning, J. Green, C. Oliveira, A. Fullerton, B. Blair, J. Kruk, G. Sonneborn, S. Penton, B. Wakker, X. Prochaska, J. Vallerga, and P. Scowen, "Unique Astrophysics in the Lyman Ultraviolet," *ArXiv e-prints*, September 2012. http://arxiv.org/abs/1209.3272 (Accessed August 2015).

[12] K. France, C. S. Froning, J. L. Linsky, A. Roberge, J. T. Stocke, F. Tian, R. Bushinsky, J.-M. Désert, P. Mauas, M. Vieytes, and L. M. Walkowicz, "The Ultraviolet Radiation Environment around M dwarf Exoplanet Host Stars," *The Astrophysical Journal*, vol. 763, no. 2, p. 149, 2013.

[13] J. B. Muhlestein, "Optical Constants for Y2O3 in the Extreme Ultraviolet." Honors Thesis, Brigham Young University, 2009.

[14] S. Lunt, "The Use of Genetic Algorithms in Multilayer Mirror Optimization." Honors Thesis, Brigham Young University, 1999.

[15] D. Y. Smith, E. Shiles, and M. Inokuti, *Handbook of Optical Constants of Solids: The Optical Properties of Metalic Aluminum*, vol. I. Academic Press, 1997.

[16] E. Fontana, R. H. Pantell, and M. Moslehi, "Characterization of dielectric-coated, metal mirrors using surface plasmon spectroscopy," *Appl. Opt.*, vol. 27, pp. 3334–3340, Aug 1988.

[17] R. P. Madden, L. R. Canfield, and G. Hass, "On the Vacuum-Ultraviolet Reflectance of Evaporated Aluminum Before and during Oxidation," *J. Opt. Soc. Am.*, vol. 53, p. 620, May 1963.

[18] E. Spiller, *Soft X-Ray Optics*. SPIE Optical Engineering Press, 1994.

[19] J. Peatross and M. Ware, *Physics of Optics and Light*. Brigham Young University, 2013 ed., May 2014.

[20] I. Newton, *Opticks: A Treatise of the Reflections, Refractions, Inflections & Colours of Light*. Dover Publications, based on 4th ed., 1952.

[21] L. G. Parratt, "Surface Studies of Solids by Total Reflection of X-Rays," *Phys. Rev.*, vol. 95, pp. 359–369, Jul 1954.

[22] M. Fox, *Optical Properties of Solids*. New York: Oxford University Press, 2 ed., 2010.

[23] Advanced Light Source, "ALS Quick Facts and New Tools." http://www-als.lbl.gov/images/stories/About_the_ALS/new-tools.pdf, August 2014. (Accessed August 2015).

[24] J. Baker, "Transition probabilities for one electron atom," Technical Note 1612, Natl. Inst. Stand. Technol., Washington, DC, 2008.

[25] D. L. Windt, "IMD - Software for modeling the optical properties of multilayer films," *Computers in Physics*, vol. 12, no. 4, pp. 360–370, 1998.

[26] M. Milosevic, *Internal Reflection and ATR Spectroscopy.* New Jersey: John Wiley & Sons, Inc., 2012.